

The Pennsylvania State University

The Graduate School

Department of Physics

# THE PERTURBATIVE STUDY OF BLACK HOLE COLLISIONS

A Thesis in

Physics

by

John Gerard Baker

© 1999 John Gerard Baker

Submitted in Partial Fulfillment  
of the Requirements  
for the Degree of

Doctor of Philosophy

May 1999

We approve the thesis of John Gerard Baker.

Date of Signature

---

Jorge Pullin  
Associate Professor of Physics  
Thesis Adviser  
Chair of Committee

---

Lee Smolin  
Professor of Physics

---

Pablo Laguna  
Associate Professor of Astronomy and Astrophysics

---

L. Samuel Finn  
Associate Professor of Physics and  
Astronomy and Astrophysics

---

Jayanth R. Banavar  
Professor of Physics  
Acting Head of the Department of Physics

## Abstract

In this work we consider the binary black hole collision problem by modelling the collision as a perturbation of the final stationary black hole spacetime. We first study head-on collisions of black holes with initial momentum or angular momentum as a perturbation of a spherically symmetric Schwarzschild black hole, the Close-Slow approximation. The results agree surprisingly well with numerical solutions of the exact Einstein equations, where such calculations are available for comparison and our linear treatment allows some interpretation of the results which is unavailable in the numerical calculations. Building on this, we examine a “two-phase” approximation which uses a combination of Newtonian limit and Close-slow approximation results to estimate the radiation energies for collisions from distant infall, showing that the estimate result is somewhat independent of how the two approximations are joined. Then, working toward the goal of performing similar perturbation treatments of black hole collisions with significant final angular momentum, we also consider the problem of determining initial values for the Teukolsky function which governs perturbations of rotating black holes. Toward this aim, we show how the Teukolsky function can be calculated from information about the initial perturbations of the metric and extrinsic curvature and then describe a proposal for deriving axisymmetric two black hole initial data with non-trivial angular momentum within the framework of a novel local solution of general relativity’s constraint equations.

## Table of Contents

List of Figures . . . . .	vii
Chapter 1. Introduction . . . . .	1
Chapter 2. Black Hole Collisions in the Close-Slow Approximation . . . . .	4
2.1 Initial Data . . . . .	4
2.2 Conformally Flat Formalism . . . . .	5
2.3 Close-Limit Initial Data . . . . .	8
2.3.1 Black Hole Configurations . . . . .	8
2.3.2 Extrinsic Curvature . . . . .	9
2.3.3 Conformal Factor . . . . .	16
2.3.3.1 Eliminating the Source Term . . . . .	17
2.3.3.2 Misner's Data . . . . .	18
2.3.3.3 Price-Pullin Approximation . . . . .	19
2.3.4 Further Considerations . . . . .	21
2.3.4.1 The Background Mass . . . . .	21
2.3.4.2 Which Close Limit? . . . . .	22
2.4 Perturbative Evolution . . . . .	24
2.4.1 Schwarzschild Perturbation Formalism . . . . .	25
2.4.2 Initial Values for $Q_{\times}$ and $Q_{+}$ . . . . .	29
2.5 Results . . . . .	33

2.5.1	Waveforms and Radiation Energy . . . . .	34
2.5.2	Results Evident Before Calculation . . . . .	36
2.5.3	Boosted Collisions . . . . .	38
2.5.3.1	Comparison with Numerical Evolution . . . . .	40
2.5.3.2	Momentum Dominance . . . . .	43
2.5.3.3	The Mass Scale Error for Large $P$ . . . . .	45
2.5.4	The Cosmic Screw . . . . .	46
2.5.5	Off-Axis . . . . .	50
2.6	Discussion . . . . .	52
Chapter 3.	Two-Phase Evolution . . . . .	55
3.1	Introduction . . . . .	55
3.2	Calculation . . . . .	59
3.3	Results . . . . .	61
Chapter 4.	Initial Data for Kerr Perturbations . . . . .	65
4.1	Calculating $\Psi_4$ . . . . .	66
4.1.1	Generic treatment . . . . .	67
4.1.2	Perturbations . . . . .	69
4.1.3	Discussion . . . . .	72
4.2	A New Approach to Kerr-Limit Data . . . . .	74
4.2.1	Solving the Constraints . . . . .	75
4.2.2	The Single Black Hole . . . . .	81
4.2.3	Two Black Holes . . . . .	84

	vi
4.2.4 Discontinuities . . . . .	88
4.2.5 Discussion . . . . .	90
Chapter 5. Future Directions . . . . .	92
Appendix. Inversion Symmetry of $\hat{K}_{ij}$ . . . . .	94
References . . . . .	97

## List of Figures

2.1 Here we give a conservative measure of the relative error in our approximation for the extrinsic curvature compared against the numerical computation. . . . . 15

2.2 This figure shows the shapes of the Misner waveform and the  $l = 2, m = 0, even$  boost waveform the destructive interference which leads to the dip in the energy curves is evident. These waveforms are evaluated at  $\bar{r} = 200M_{Sch}$ . . . . . 39

2.3 Here we show the energy as a function of momentum for several choices of separation. The dip in energy arising from cancellation between the Misner and momentum parts of the waveform is clearly evident. The fully nonlinear numerical result is included for comparison. Reproduced from Ref. [19] with permission. Copyright ©1997 by the American Physical Society. . . . . 41

2.4 These are waveform comparisons, evaluated at  $\bar{r} \sim 15M_{Sch}$  with  $\mu_0 = 1.0$  for several relatively small values of  $P/M$ . Note the agreement between the linear and nonlinear calculations. . . . . 42

2.5 This figure shows the inversion of the linear wave forms from boosted black hole collisions as the initial momentum is increased. The partial cancellation results in a dip in the radiation energy as the momentum increases. These waveforms have been evaluated at  $\bar{r} = 200M_{Sch}$ . . . . . 44

2.6	Here we show a superposition of 19 “momentum parts” from the numerical waveforms rescaled to allow for the momentum dependence of the initial mass. The excellent match suggests linear dynamics despite the disagreement between the linear and numerical energies at large momenta. A linear momentum part is also shown for comparison. The waveforms were evaluated at $\bar{r} \sim 15M_{Sch}$ .	47
2.7	The cosmic screw $l = 2, m = 0$ odd-parity momentum part waveform evaluated at $\bar{r} = 200M_{Sch}$ .	48
2.8	The radiation energy curves for the cosmic screw configuration with estimated corrections to account for the mass under-estimate in our treatment.	49
2.9	Here we show a comparison of the radiation energy dependence on spin and orbital angular momentum. A notable feature is that the dependence on $J$ is independent of the separation.	51
2.10	Here we show the radiation energy dependence on the initial angle of the linear momentum away from the inward direction. The inward component results in a dip at low values of $J$ . The crossing-over of the curves is a consequence of the transition to momentum dominance.	53
3.1	A cartoon illustration of how the two-phase approximation is constructed.	56



- 3.2 Here we see that the amount of radiated energy is not sensitive to the choice of transition. The horizontal axis indicates the separation at which we switch from Newtonian to close-limit evolution. The curves show results for the radiation according to the two-phase approximation for collisions of black holes released from several different initial separations,  $\mu_0$ . It is evident that for holes released from significant initial distances the radiation result is not sensitive to the choice of transition as long as the transition is made somewhere in the vicinity of the separation at which a horizon first forms. . . . . 62
- 3.3 This plot shows the excellent agreement of the two-phase approximation with the numerical result. The error estimates shown with the two-phase data are based on our analysis of the sensitivity of these results to the choice of separation at which we switch methods of evolution. . . . . 63

## Chapter 1

### Introduction

Considering that black holes are the fundamental compact objects of general relativity, it immediately becomes interesting to wonder: What happens when two black holes interact? What happens when black holes collide? While solitary black holes have impressive simplicity, their collisions are profoundly complicated, still troubling numerical relativists who have been working many years to have supercomputers calculate the interaction. The general process of a typical black hole collision begins with a long inspiral stage during which the black holes orbit each other and slowly radiate gravitational wave energy, falling closer together and accelerating until they are so close that orbits are no longer possible. At this point we expect the black holes to plunge together to form a single hole. The new hole starts out highly distorted and will go through a series of undulations, radiating more gravitational energy until it settles down to a final simple state. Throughout the entire process the pair is sending out gravitational waves.

Here on Earth researchers in several countries are constructing instruments that will be able to listen for gravitational waves.[1] Binary black hole collisions are expected to be one of the most significant sources of detectable gravitational waves producing perhaps as many as several events per year with the aid of sensitive new instruments beginning operation in the next few years.[2] These new astronomical devices will provide us with a new type of information about the universe around us. The detection of the

gravity wave signal that comes from a binary black hole collision may someday constitute final indisputable proof of the existence of black holes.[3]

But what would such a signal look like? Intensive efforts are underway to numerically calculate black hole collisions[4, 5] and progress is coming, but with such a difficult problem it is important to have an alternative means of calculation against which to check results. Black hole perturbation studies can fulfill this role as well as provide some explanations of what is going on in the numerical results. Since the final result of a black hole collision is simply a single black hole it is appropriate to treat the last details of a black hole collision as the linear dynamics of a single perturbed black hole. Price and Pullin[6] have treated the problem of head-on binary black hole collisions with the holes released initially close and from rest as perturbations of the spherically symmetric Schwarzschild black hole. They found agreement with comparable fully non-linear numerical supercomputer calculations up to unexpectedly far apart initial separations.

In Chapter 2, the largest part of this work, we consider an extension of their Schwarzschild perturbation method to the case of black holes which have some initial motion, the so-called Close-Slow approximation. We also find a wide domain of agreement with numerical calculations and are able to explain features of the numerical results that were otherwise mysterious. In Chapter 3 we take advantage of some results from Chapter 2 to evaluate a method for estimating the amount of radiation energy from a collision of black holes which are initially far apart based on the results for initially close black holes. Since inspiral collisions will produce a final black hole with angular momentum, it will be most appropriate to treat the dynamics of this type of collision as

a perturbation of a spinning Kerr black hole. In Chapter 4 we consider the problem of specifying initial data for Kerr perturbation studies.

## Chapter 2

### Black Hole Collisions in the Close-Slow Approximation

In this chapter we will extend the work of Price and Pullin[6] on close-limit collisions of initially stationary black holes to consider collisions of black holes with initial momentum or spin. In the first three sections we discuss the initial data which we will use to represent initial configurations of moving black holes. This is followed by an exposition of the Schwarzschild perturbation technique in §2.4. The last two sections present the results including a comparison with numerical calculations and some closing discussion.

#### 2.1 Initial Data

Before beginning any 3+1 approach to calculating an approximate spacetime which includes colliding black holes it is necessary to specify appropriate initial data. This of course means that we must construct a 3-metric  $g_{ij}$  and extrinsic curvature  $K_{ij}$  which satisfy the constraint conditions implied on the initial slice from the full set of Einstein's equations. The most widely used method for solving the constraints in black hole collision problems is the conformally flat formalism developed by York and others.[7, 8] Numerical solutions of the constraints within this formalism were worked out by Cook[9, 10] and others and are now used routinely in numerical simulations of binary black hole collisions. Since one of the primary motivations of the close limit approach

is to provide benchmarks for numerical studies, we will be applying this common conformally flat family of initial data for the Schwarzschild perturbation studies. Although it would be possible to apply an Schwarzschild perturbation approach to evolve the exact numerical solutions[11] for initial values within this family that represent sufficiently close black holes, it is more advantageous to find an approximation of these data with simple dependence on the parameters which describe the initial black hole configuration (*e.g.* momenta, separation, masses). This feature is crucial for achieving some understanding in the analysis of the resulting dynamical behavior. In the following sections we first give a general description of the conformal formalism and then present the close approximation initial data solutions for the extrinsic curvature and the conformal factor.

## 2.2 Conformally Flat Formalism

The conformal formalism begins by making the simplifying assumptions that the 3-metric is conformally related to a flat metric,  $\hat{g}_{ij}$ ,

$$g_{ij} = \psi^4 \hat{g}_{ij} \tag{2.1}$$

and that the extrinsic curvature is traceless

$$K_{ij} g^{ij} = 0. \tag{2.2}$$

To simplify the resulting constraint equations a conformal extrinsic curvature is also defined,

$$K_{ij} = \psi^{-2} \hat{K}_{ij} K^{ij} = \psi^{-10} \hat{K}^{ij} \quad (2.3)$$

for which Eq. 2.2 implies

$$\hat{K}_{ij} \hat{g}^{ij} = 0. \quad (2.4)$$

In terms of these quantities the momentum constraint decouples from the Hamiltonian constraint, becoming

$$\hat{\nabla}_j \hat{K}_i^j = 0, \quad (2.5)$$

and the Hamiltonian constraint simplifies to

$$\hat{\nabla}^2 \psi = -\frac{1}{8} \psi^{-7} \hat{K}_{ij} \hat{K}^{ij} \quad (2.6)$$

where all quantities with a hat are related to the flat conformal space. The strategy then is to solve Eq. 2.5 first to find a family of solutions for  $\hat{K}_{ij}$ . Afterwards using the appropriate solution in the source term on the right-hand side of 2.6, the Hamiltonian constraint becomes a non-linear elliptic problem for  $\psi$ . Bowen and York [8] found momentum constraint solutions for  $\hat{K}_{ij}$  which represent one black hole with momentum,  $P^i$ , and angular momentum,  $J^i$ . They showed that

$$\hat{K}_{ij}^{one}(P^i) = \frac{3}{2r^2} [P_i n_j + P_j n_i - (\hat{g}_{ij} - n_i n_j) P^k n_k] \quad (2.7)$$

satisfies Eq. 2.5 and as conformal extrinsic curvature gives the slice and ADM momentum  $P^i$ . It is simply related to the black hole's location in conformal space by  $r$  and  $n^i$ , the conformal distance from the hole and the conformal unit vector directed radially away from the hole. To describe rotating holes they found another solution

$$\hat{K}_{ij}^{one}(J^i) = \frac{3}{r^3}[\epsilon_{kil}J^l n^k n_j + \epsilon_{kjl}J^l n^k n_i] \quad (2.8)$$

which gives the spatial slice ADM angular momentum,  $J^i$ . It should be noted that these spinning Bowen-York type black hole are not Kerr black holes. The Kerr metric does not have conformally flat slices (at least not in the Boyer Lindquist foliation). This difference has been explored in the context of the close approximation by other researchers.[12] Because the momentum constraint is linear in  $\hat{K}_{ij}$  it makes sense to add solutions for multiple black holes:

$$\hat{K}_{ij}^{two} = \hat{K}_{ij}^{one}(P_1^i, J_1^i, r_1, n_1^i) + \hat{K}_{ij}^{one}(P_2^i, J_2^i, r_2, n_2^i). \quad (2.9)$$

With  $\hat{K}_{ij}$  specified the remaining step is to solve Eq. 2.6 for the conformal factor  $\psi$ . To find  $\psi$  one must impose boundary conditions. While it is obvious that we should set  $\psi \rightarrow 1$  at infinity, choosing an inner boundary condition can be more complicated. Typically an inversion symmetry is imposed which specifies that the spatial slice has the form of two isometric sheets joined at spherical throats for each black hole. The inversion mapping is realized in the conformal space by inversion through the spherical throats centered at  $r_1$  and  $r_2$ . The relative sizes chosen for the spheres will be related to



the relative masses of the holes. The symmetrization is then accomplished by a method of images based on this inversion mapping. In cases where the inversion symmetric boundary conditions imposed for Eq. 2.6 a corresponding symmetry is imposed on  $\hat{K}_{ij}$ . The symmetrized  $\hat{K}_{ij}$  is obtained from a method of images again beginning from the basic Bowen-York solution Eq. 2.9.

### 2.3 Close-Limit Initial Data

In this work we will be approximating the inversion symmetric data, but it should also be noted that other inner boundary conditions are also available and occasionally used in practice. In particular, Brandt and Brügmann[13] have described a boundary condition which is more convenient for some numerical calculations and has also been useful in working out second order Schwarzschild perturbations for black hole collisions.[14]

#### 2.3.1 Black Hole Configurations

Now we seek to approximate Bowen-York type initial data with the isometry boundary condition. We will specify for our calculations that the the black holes have equal mass. That case has seen the most interest in numerical evolution studies and is a good starting point for perturbative studies. Our approach is easily extendible to allow differing masses, and other researchers have considered the case of perturbative evolutions of from initially static Misner black holes with unequal masses.[15] Since perturbative investigations from Misner data, for black holes with no initial momentum or spin, have been completed by others we will be primarily interested in extending those results for the case of black holes with some small amount of initial linear and angular

momentum. We require that the initial ADM linear momentum vanishes which means that the momentum parameters of the black holes will be equal and opposite,  $P_1^i = P_2^i$ . We also restrict to cases in which the angular momentum parameters for the black holes are equal and opposite,  $J_1^i = J_2^i$ , though it should be noted that this does not mean the ADM angular momentum will necessarily vanish as there may also be some “orbital” angular momentum, and we will consider the case where some small amount of orbital angular momentum is present.

In principle five parameters would be required to describe the possible arrangements of linear and angular momenta of the class of systems we are studying. In this work though we will only consider three of these parameters in detail, making only a few comments about the expected dependence on the other two. We will study most closely the dependence on the inward component of the linear momentum,  $P_{\parallel}$ , and we will also consider the initial component of the momentum that is perpendicular to the erstwhile symmetry axis,  $P_{\perp}$ , and the inward component of the spin angular momentum directed along the symmetry axis  $J_{\parallel}$ . The other two components needed to complete the picture are the components of the spin angular momentum perpendicular to the axis and either parallel or perpendicular to  $P_{\perp}$ . Investigations of these other parameters have been carried out in collaboration with Hans Peter Nollert, but these are not discussed in detail here.

### 2.3.2 Extrinsic Curvature

The close approximation for the extrinsic curvature is based on the observation from the Bowen-York form of the extrinsic curvature that when the two black holes

have opposing linear and angular momenta, there is a near cancellation if the combined extrinsic curvature is evaluated far from the two throats. If we suppose that the black holes are located on the  $z$  axis in the conformal space and are centered around the origin but separated by a conformal distance  $L$  so that,

$$\mathbf{r}_1 = \mathbf{r} + \frac{L}{2}\hat{\mathbf{z}} \quad (2.10)$$

and

$$\mathbf{r}_2 = \mathbf{r} - \frac{L}{2}\hat{\mathbf{z}}, \quad (2.11)$$

then

$$r_1 \simeq r + \frac{zL}{2r} \quad (2.12)$$

$$r_2 \simeq r + \frac{zL}{2r} \quad (2.13)$$

and

$$\mathbf{n}_1 = \mathbf{n} + \frac{1}{2}\frac{L}{r}(\hat{\mathbf{z}} - \frac{z}{r}\hat{\mathbf{n}}) \quad (2.14)$$

$$\mathbf{n}_2 = \mathbf{n} - \frac{1}{2}\frac{L}{r}(\hat{\mathbf{z}} - \frac{z}{r}\hat{\mathbf{n}}). \quad (2.15)$$

To define the close limit we specify that “close” means that the conformal separation of the black holes is much less than the mass of the Schwarzschild spacetime we are perturbing,  $L \ll M_{Sch}$ . Since we are only interested in the region outside the horizon of the Schwarzschild black hole we will only need data for the region  $r > M_{Sch}$ . In terms

of the conformal space, if the throat radii are kept constant and the holes are brought closer together, the ADM mass of the slice increases, blowing up when the throats just touch. Then  $r > M_{Sch} \gg L$  so  $\frac{L}{r} \ll 1$ . In this limit it is clear that

$$r_1 \sim r_2 + \mathcal{O}\left(\frac{L}{r}\right) \quad \text{and} \quad (2.16)$$

$$\mathbf{n}_1 \sim \mathbf{n}_2 + \mathcal{O}\left(\frac{L}{r}\right). \quad (2.17)$$

On the other hand we have chosen to consider the case that the holes have opposite linear and angular momenta,

$$P_1^i = -P_2^i \quad (2.18)$$

$$J_1^i = -J_2^i. \quad (2.19)$$

If each black hole is to have some combination of linear and angular momenta then the Bowen York solution for the conformal extrinsic curvature tensor corresponding to each black hole is

$$\begin{aligned} \hat{K}_{1,2ij} = & \frac{3}{2r_{1,2}^2} [P_{1,2i} n_{1,2j} + P_{1,2j} n_{1,2i} - (\hat{g}_{ij} - n_{1,2i} n_{1,2j}) P_{1,2}^k n_{1,2k}] \\ & + \frac{3}{r_{1,2}^3} [\epsilon_{kil} J_{1,2}^l n_{1,2}^k n_{1,2j} + \epsilon_{kjl} J_{1,2}^l n_{1,2}^k n_{1,2i}]. \end{aligned} \quad (2.20)$$

Taking into account the close limit comparisons of  $r, n^i, P^i$  and  $J^i$  for each hole described above it is clear that

$$\hat{K}_{1ij} = -\hat{K}_{2ij} + \mathcal{O}\left(\frac{L}{r}\right) \quad (2.21)$$

so that the combined conformal extrinsic curvature will be of order  $\frac{L}{M_{Sch}}$ .

$$\hat{K}_{ij} = \hat{K}_{1ij} + \hat{K}_{1ij} \simeq \mathcal{O}\left(\frac{L}{r}\right). \quad (2.22)$$

As with the Schwarzschild metric  $K_{ij}$  vanishes in the  $\frac{L}{M_{Sch}} \rightarrow 0$  limit. This justifies an attempt to apply Schwarzschild perturbation theory to the case of black holes with momentum. Notice that we have not yet needed to make any assumptions about the size of the linear and angular momentum parameters relative to  $M_{Sch}$ . For any  $P^i$  and  $J^i$ ,  $L$  can be chosen so that the deviation from the Schwarzschild extrinsic curvature is as small as we need for linear behavior in the evolution.

Since the extrinsic curvature depends linearly on the momentum components we can split it up into pieces which each depend on only one component,

$$\hat{K}_{ij} = P_{\parallel} \hat{K}_{ij}^{\text{Boost}} + J_{\parallel} \hat{K}_{ij}^{\text{Screw}} + P_{\perp} \hat{K}_{ij}^{\text{Off-Axis}}. \quad (2.23)$$

The labels indicate the names we use in referring to the three types of collisions in which all but one linear or angular momentum component vanishes, head-on “boosted” black hole collisions, head-on twisting “cosmic screw” collisions, and slightly “off-axis” collisions which have some ADM angular momentum of  $\mathcal{O}\left(\frac{L}{M}\right)$ .

In Cartesian coordinates with the holes placed on the z-axis we have for the first hole

$$r_1 = \sqrt{x^2 + y^2 + \left(z - \frac{L}{2}\right)^2} \quad (2.24)$$

$$\mathbf{n}_1 = \left( \frac{x}{r_1}, \frac{y}{r_1}, \frac{z}{r_1} \right). \quad (2.25)$$

Restricting to on-axis spins and choosing the  $x$ -axis to be in the direction of  $P_\perp$ , the linear and angular momenta are,

$$\mathbf{P}_1 = (P_\perp, 0, -P_\parallel) \quad (2.26)$$

$$\mathbf{J}_1 = (0, 0, J_\parallel). \quad (2.27)$$

The same formulae apply for the quantities related to the second hole but with  $L \rightarrow -L$ ,  $P_\parallel \rightarrow -P_\parallel$ ,  $P_\perp \rightarrow -P_\perp$ ,  $J_\parallel \rightarrow -J_\parallel$ . As described above we take Eq. 2.20 to give the conformal extrinsic curvature for each black hole. Then adding for the two black hole solution and keeping only the  $\mathcal{O}(\frac{L}{M})$  part leaves a rather complicated expression in terms of  $x$ ,  $y$ , and  $z$ . We will ultimately want to expand these expressions in terms of spherical harmonics which is more natural in spherical coordinates,  $r$ ,  $\theta$  and  $\phi$ . Fortunately this also simplifies the expressions. The result, split into the pieces defined in Eq. 2.23, is

$$\begin{aligned} \hat{K}_{ij}^{\text{Boost}} &= \frac{3L}{r^3} \begin{pmatrix} -2 \cos(\theta)^2 & 0 & 0 \\ 0 & \frac{r^2 (3 + \cos(2\theta))}{4} & 0 \\ 0 & 0 & \frac{r^2 (1 + 3 \cos(2\theta)) \sin(\theta)^2}{4} \end{pmatrix} \\ \hat{K}_{ij}^{\text{Screw}} &= \frac{3L}{r^4} \begin{pmatrix} 0 & 0 & -4r \cos(\theta) \sin(\theta)^2 \\ 0 & 0 & -(r^2 \sin(\theta)^3) \\ -4r \cos(\theta) \sin(\theta)^2 & -(r^2 \sin(\theta)^3) & 0 \end{pmatrix} \end{aligned} \quad (2.28)$$

$$\hat{K}_{ij}^{\text{Off-Axis}} = \frac{3L}{r^3} \begin{pmatrix} \sin(2\theta) \sin(\varphi) & r \sin(\varphi) & \frac{r \cos(\varphi) \sin(2\theta)}{2} \\ r \sin(\varphi) & -\left(\frac{r^2 \sin(2\theta) \sin(\varphi)}{4}\right) & \frac{r^2 \cos(\varphi) \sin(\theta)^2}{2} \\ \frac{r \cos(\varphi) \sin(2\theta)}{2} & \frac{r^2 \cos(\varphi) \sin(\theta)^2}{2} & \frac{-3 r^2 \cos(\theta) \sin(\theta)^3 \sin(\varphi)}{2} \end{pmatrix}$$

In principle the next step is to calculate the symmetrized form of  $\hat{K}_{ij}$  so that the inversion isometry used as a boundary condition for the Hamiltonian constraint corresponds to a physical symmetry of the spacetime slice. In the close limit case though the symmetrization turns out to be irrelevant to  $\mathcal{O}(\frac{J}{M})$  so that Eq. 2.28 will be the final form of the conformal extrinsic curvature. This point is argued in more detail in the appendix. We have numerically verified the ‘‘Boost’’ part of our extrinsic curvature approximation. In Fig. 2.1, we show the difference between the approximate and numerically calculated results conservatively measured by the maximum component difference found in the  $r = 2m$  sphere, and plotted at various separations.

The figure shows a difference of 10% only at separations no less than  $\mu_0 = 1.5$ . The parameter  $\mu_0$  is a measure of separation described below. When the momentum is small, the holes are surrounded by a common event horizon when  $\mu_0 \sim 1.8$  or less.

Notice that in all of the discussion so far for the close approximation of  $\hat{K}_{ij}$  we have not had to make any assumptions about the size of the linear or angular momenta of the holes. No linearization is required with respect to the momentum parameters because the exact conformal formalism  $\hat{K}_{ij}$  is homogeneously linear in these parameters. An assumption about the size of these parameters will, however, be needed later when we solve the Hamiltonian constraint.

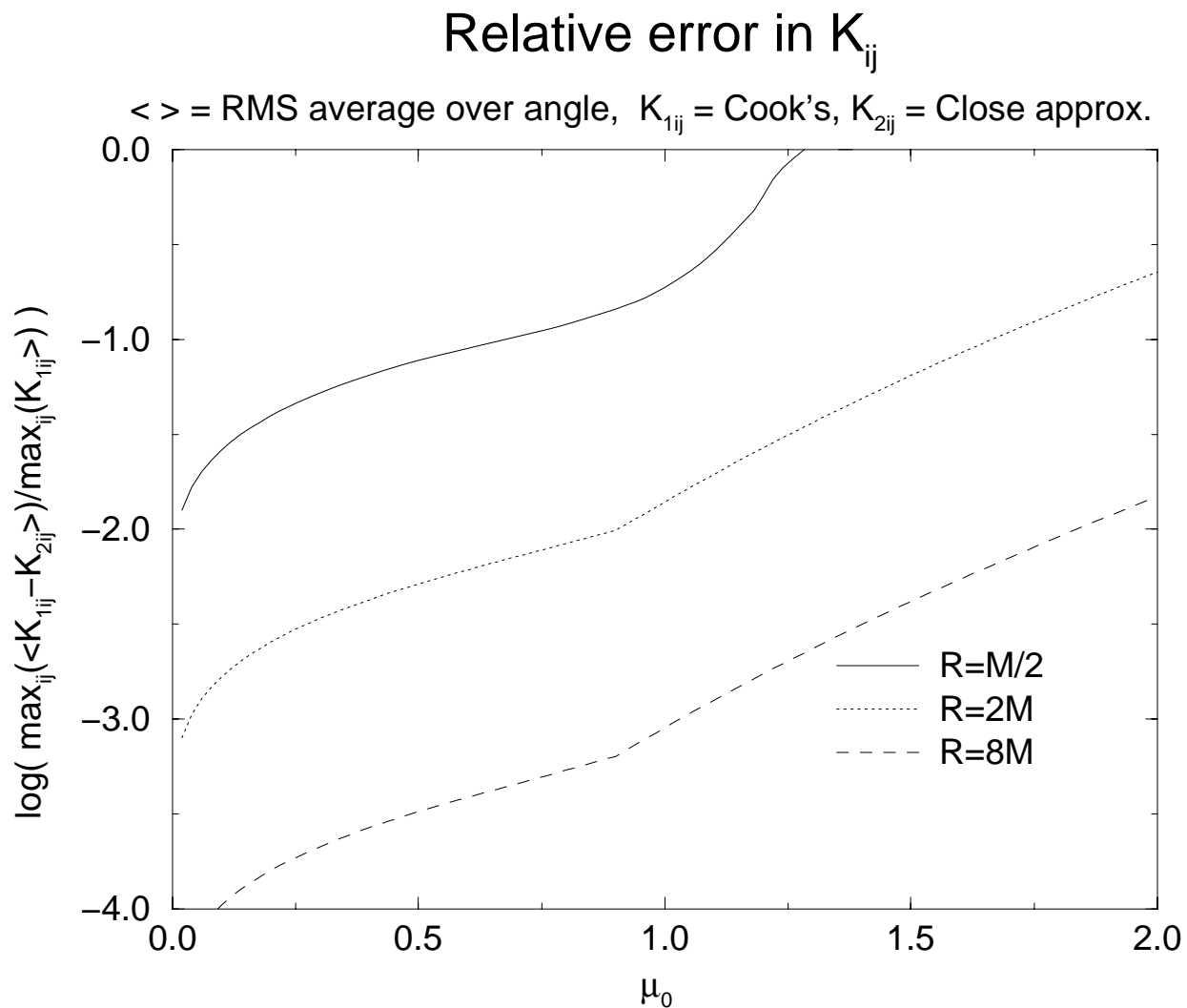


Fig. 2.1. Here we give a conservative measure of the relative error in our approximation for the extrinsic curvature compared against the numerical computation.



It is worth pointing out here also that although the formulas given in Eq. 2.28 are only approximate representations of the standard solutions of the conformal formalism, they are nonetheless exact solutions of the momentum constraint. This is essentially a consequence of the linearity of the momentum constraint. It is apparent that if the momentum parameters are chosen proportional to  $M/L$ , then terms of higher order in  $\frac{L}{M}$  vanish in the  $\frac{L}{M} \rightarrow 0$  limit, yet the terms in Eq. 2.28 remain as finite exact solutions. This is particularly interesting in the case of  $\hat{K}_{ij}^{\text{Off-Axis}}$ , since it carries angular momentum and might be considered as an alternative to the Bowen-York spinning black hole solution.

### 2.3.3 Conformal Factor

With a solution of the momentum constraint in hand, the next step is to solve the Hamiltonian constraint

$$\hat{\nabla}^2 \psi = -\frac{1}{8} \psi^{-7} \hat{K}_{ij} \hat{K}^{ij} \quad (2.29)$$

for the conformal factor  $\psi$ . If we take the viewpoint that we are looking for solution to this nonlinear elliptic equation in the region of the conformal space outside the throats, then we need to impose boundary conditions at  $r \rightarrow \infty$  and at the throats. At infinity it is simplest to require  $\psi \rightarrow 1$  so that the conformal space asymptotically approaches the physical space. The inner boundary condition is implied by the inversion isometry, and is manifest by a method of images. While this elliptic equation is routinely solved in numerical studies, we again want to seek out an approximation which maintains simple parameter dependence.

### 2.3.3.1 Eliminating the Source Term

If the source term in Eq. 2.29 vanished identically then we would have the same equation and the same elliptic problem as for the case of black holes initially at rest. The case of black holes at rest with inversion symmetry has a well known solution found by Misner[16]. Considering the source term while looking at our solution for  $\hat{K}_{ij}$ , Eq. 2.28, it is tempting to argue that, since our  $\hat{K}_{ij}$  is of order  $\frac{L}{M}$ , the source term will be of order  $(\frac{L}{M})^2$ , negligible in the close limit without any consideration of the momentum. This would not be correct though because the boundary problem requires evaluating the source term all the way up to the throats. In the region near the throats the assumption that  $r \gg L$  used in the derivation of Eq. 2.28 does not hold, thus our solutions do not correspond to the standard conformal formalism solutions in that region. Although it is certainly appropriate to use our momentum constraint solutions in the source term where  $r > m$  we must understand  $\hat{K}_{ij}$  to refer to the exact solution in the inner region near the throats. We resolve this by requiring that the magnitude of the holes' linear and angular momenta be small. The standard solution for  $\hat{K}_{ij}$  as well as ours are linear in the momentum. Choosing the momenta of order  $\frac{L}{M}$  we can guarantee that the source term is quadratic in  $\frac{L}{M}$  everywhere and hence the difference between the solution of our boundary value problem and the Misner solution will be quadratic in  $\frac{L}{M}$  as well. What this analysis show is that we can choose the magnitudes on the linear and angular momenta sufficiently small so that the Misner solution still appropriate. Thus for our data we take the conformal factor to be the one found by Misner.

### 2.3.3.2 Misner's Data

The line element for the metric in Misner's initially stationary black hole solution is

$$ds_{Mis}^2 = A^2 \psi_{Mis}^4 \left[ d\mu^2 + d\eta^2 + \sin^2 \eta d\phi^2 \right] \quad (2.30)$$

where

$$\psi_{Mis} = \sum_{n=-\infty}^{n=\infty} \frac{1}{\sqrt{\cosh(\mu + 2n\mu_0) - \cos \eta}} \quad (2.31)$$

and  $A$  is a scaling constant. To cover the region outside the throats in the equal mass case, the bispherical coordinates  $\mu$  and  $\eta$  range  $-\mu_0 \leq \mu \leq \mu_0$  and  $0 \leq \eta \leq \pi$ . These data have the inversion isometry property with respect to the throats located at  $\mu = \mu_0$  and  $\mu = -\mu_0$ . Thus,  $\mu_0$  determines how close the holes are. These bispherical coordinates are related to spherical coordinates by

$$\begin{aligned} r &= A \sqrt{\frac{\cosh \mu + \cos \eta}{\cosh \mu - \cos \eta}} \\ \theta &= \frac{\sin \eta}{\sinh \mu} \end{aligned} \quad (2.32)$$

We have already mentioned that the Misner solution is a special case of the conformal formalism data with vanishing extrinsic curvature. By matching the location of the throats in the two formalisms we can figure out the relationship between the pairs of parameters  $(A, \mu_0)$  of the Misner metric and  $(a, L)$  of the conformally flat framework. We can relate these parameters by comparing the location of the spherical throats in each formalism. In the Misner data, the near poles of the throats at  $\mu = \pm\mu_0$  are located at  $\eta = \pi$  and the far poles are located at  $\eta = 0$ . In the conformal framework then the

distance between the bispherical points  $(\mu_0, \pi)$  and  $(\mu_0, 0)$  should be the diameter of the throat,  $2a$ . The distance between the near points on the two throats  $(\mu_0, \pi)$  and  $(-\mu_0, \pi)$  should be  $L - 2a$ . These imply the relations,

$$a = \frac{A}{\sinh \mu_0} \quad (2.33)$$

and

$$L = 2A \coth \mu_0. \quad (2.34)$$

### 2.3.3.3 Price-Pullin Approximation

Though the Misner data are given by an analytic expression, Eq. 2.30, the expression includes a function defined by an infinite sum. Again, for the close approximation, we want expressions with simple dependence on the parameters. In their close approximation study of black hole collisions beginning from rest, Price and Pullin have worked out a close approximation for the Misner conformal factor. Changing to spherical coordinates, the Misner metric can be put in the conformal form,

$$ds_{Mis}^2 = \psi^4 \left[ dr^2 + r^2 d\theta^2 + r^2 \sin^2 \theta d\phi^2 \right]. \quad (2.35)$$

To lowest order they find that the conformal factor for the conformally flat form of the metric can be written as

$$\psi = \left( 1 + \frac{M_{Mis}}{2r} \right) \mathcal{F} \quad (2.36)$$

with  $\mathcal{F}$  given by

$$\mathcal{F} = 1 + \left(1 + \frac{M_{Mis}}{2r}\right)^{-1} \kappa_2 \left(\frac{M_{Mis}}{r}\right)^3 (3 \cos^2 \theta - 1). \quad (2.37)$$

Here only  $M_{Mis}$  and the perturbation parameter  $\kappa_2$  depend on  $\mu_0$  and only  $M_{Mis}$  depends on the parameter  $A$ .  $M_{Mis}$  is the ADM mass of the Misner data slice. At fixed mass the perturbation parameter  $\kappa_2$  contains the  $\mu_0$  dependence, and controls the separation,  $\frac{L}{M}$ , of the throats. These quantities are defined by the relations

$$M_{Mis} = 4A\Sigma_1 \quad \text{and} \quad (2.38)$$

$$\kappa_2 = \frac{\Sigma_1 + \Sigma_3}{(4\Sigma_1)^3} \quad (2.39)$$

where

$$\Sigma_i = \sum_{n=1}^{\infty} \frac{1}{(\sinh n\mu_0)^i}. \quad (2.40)$$

For comparison, the line element of the background Schwarzschild metric in isotropic coordinates is

$$ds^2 = \left(1 + \frac{M_{Sch}}{2r}\right)^4 \left[dr^2 + r^2 d\theta^2 + r^2 \sin^2 \theta d\phi^2\right]. \quad (2.41)$$

A close look at Eq. 2.36 and Eq. 2.37 reveals that when  $\kappa_2 \rightarrow 0$  the remaining part of the conformal factor,  $\psi$ , is just  $1 + \frac{M_{Mis}}{2r}$ . If  $M_{Mis} = M_{Sch}$  then this is exactly the conformal factor in the Schwarzschild metric. It is also clear that the part of the conformal factor linear in  $\kappa_2$  has quadrupolar angular dependence.

### 2.3.4 Further Considerations

Here we look a little more closely at some details of our initial data approximation which encompass both the extrinsic curvature and the conformal factor. We seek to clarify more precisely what is the background metric and what is the “close limit”.

#### 2.3.4.1 The Background Mass

Though it is clear that our background metric is a Schwarzschild metric, we have not specified its mass,  $M_0$ . Though varying  $M_0$  only amounts to a rescaling, the matter is not trivial because our initial data are not automatically scaled by  $M_0$ . The relationship between the scales must be specified.

In our case we physically expect the perturbations to radiate quickly away leaving us with a spherically symmetric black hole indefinitely thereafter. The background metric should then represent that end-state black hole. Ideally then  $M_0$  should be the final mass of the black hole. Realistically this is determined only by evolution. The final mass, however, should differ from the initial mass by the energy radiated away during the coalescence. Where a linear perturbation approach is appropriate this radiation should be small. The linear rescaling of the mass amounts to a monopole,  $l = 0$  perturbation of the metric and does not affect the quadrupole  $l = 2$  radiation at first order. As long as the mass of the radiation is small compared to the total mass it is appropriate to take  $M_0 = M_i$  where  $M_i$  is the *initial* mass of the slice. This mass,  $M_i$ , must be computationally related to the parameters which specify the conformal data,  $a$ ,  $L$  and the momentum parameters.

It is important now to also recall that we are using an approximate form of the symmetrized conformal formalism data. In principle  $M_i$  is the exact mass of the initial slice. This mass can be calculated from the numerical solution of the constraints. Again, though, we adopt the viewpoint that an approximation is better because it will allow us to clearly see the parameter dependence. We can think of the initial mass  $M_i$  as comprised of the individual rest masses of the holes less some gravitational binding energy which depends on the separation and plus some kinetic energy which depends on the momentum. Since the mass depends directly on the conformal factor, the arguments given in §2.3.3 imply now that  $M_i$  will be the same as the Misner data mass  $M_{Mis}$  up to the kinetic energy term which is second order in the momentum

$$M_i = \chi M_{Mis} \tag{2.42}$$

$$\chi = 1 + \mathcal{O}(P^2) + \mathcal{O}(J^2). \tag{2.43}$$

Since we have already required that the momentum is small in solving the Hamiltonian constraint it is consistent to use  $\chi = 1$ . This allows us to maintain simple dependence on the parameters. We will, however, find *a posteriori* that the range of accuracy of the close approximation can be extended considerably by using the exact value for  $\chi$ .

#### 2.3.4.2 Which Close Limit?

The reader may have noticed that we have treated the solution of the momentum constraint and the solution of the Hamiltonian constraint with different ideas of what constitutes “close” black holes. In the first case we have effectively expanded in terms

of  $\frac{L}{r}$  which is less than or close to  $\frac{L}{M}$ , but in the second case the expansion parameter is  $\kappa_2$ . Here we will clarify the relationship between these parameters.

If we understand “ $M$ ” to be  $M_{Mis}$  as discussed in the last section, then from Eq. 2.38 and Eq. 2.34 we have

$$\frac{L}{M} \sim \frac{L}{M_{Mis}} = \frac{\cosh \mu_0}{2\Sigma_1}. \quad (2.44)$$

In the small  $\mu_0$  limit  $\coth \mu_0 \sim 1/\mu_0$  and Price and Pullin showed that  $\Sigma_1 \sim \frac{|\ln \mu_0|}{\mu_0}$  so that

$$\frac{L}{M} \sim |\ln \mu_0|^{-1} \equiv \epsilon. \quad (2.45)$$

The second relation is the definition of  $\epsilon$ . Likewise, Price and Pullin have shown that  $\kappa_2$  behaves in the close limit as

$$\kappa_2 \propto |\ln \mu_0|^{-3} = \epsilon^3. \quad (2.46)$$

This means that in the extreme close limit

$$\kappa_2 \propto \left(\frac{L}{M}\right)^3. \quad (2.47)$$

We will allow this seeming inconsistency to persist. In most cases we will find that the “conformal factor” contributions and the “momentum” contributions are essentially never added together. In cases where comparison of the magnitudes of these contributions are important we want to be able to consider a full range of values for  $P$  and  $J$  from zero at least up to  $\mathcal{O}(\frac{L}{M})$ . For sufficiently small  $P$  and  $J$  the metric perturbations will be larger than the extrinsic curvature perturbations, but as long as the size of the momentum parameters is at least of order  $\frac{L}{M}$ , the extrinsic curvature contribution will



be more important. We will return to this important point in the discussion of the results.

## 2.4 Perturbative Evolution

As we have motivated it should be appropriate to treat the black hole collision spacetime as a linear perturbation of the Schwarzschild spacetime for sufficiently later stages in the coalescence. In our case we model these “late stages” by beginning with initial data from the family of approximate constraint solutions described above with the parameters chosen to represent sufficiently close, slow-moving black holes. For our approximate data, as for the exactly calculated conformally flat data, the limit  $\frac{L}{M} \rightarrow 0$  reproduces Schwarzschild data on a Killing time slice. If  $\frac{L}{M}$  is increased slightly away from zero, then the data represent a slightly non-spherical black hole with some extrinsic curvature on the initial slice. Linear evolution will tell us how these deviations propagate in time on the Schwarzschild background.

The perturbative approach to general relativity begins by supposing a parameterized family of spacetime metrics which gives a known spacetime solution of Einstein’s equations when the parameter goes to zero. By analytic expansion of the metric in terms of this parameter, Einstein’s equations can be broken up into a series of terms proportional to different powers of the expansion parameter. The condition that the linear coefficient of the expansion parameter in Einstein’s equations vanishes gives a set of linear perturbation equations. Finding a solution of these equations gives a parameterized family of metrics with the property that varying the parameter from zero changes the

metric *before* changing the value of the Einstein tensor. Then it is reasonable to expect that an exact solution exists which resembles the linearized solution as long as the parameter is sufficiently small. In our case the background is the Schwarzschild spacetime. The perturbative family of metrics are obtained as solutions of the linear evolution equations given below for the Regge-Wheeler and Zerilli functions so that the linear coefficient of Einstein's equations will be satisfied. And this family is parameterized by the separation of the black holes,  $\frac{L}{M}$ . The additional parameters representing momentum can be thought of as labels for an extended set of families which all satisfy the linearized equations. In the §2.4.1 and §2.4.2 we briefly describe the general formalism for treating perturbations of the Schwarzschild spacetime then discuss the specifics of the close black hole collision problem.

### 2.4.1 Schwarzschild Perturbation Formalism

The case of perturbations of the Schwarzschild solution was studied in detail by Regge and Wheeler who simplified the evolution equations for “odd-parity” perturbations. Zerilli followed up on their work with a simplification for the remaining “even-parity” perturbations. Later Moncrief specified an encompassing formalism which did not require assumptions about the gauge of the metric perturbations. We will apply Moncrief's formalism to the black hole collision problem, describing only the details necessary for understanding the results.

In general the perturbative form of Einstein's equations should constitute a system of linear equations in 3+1 dimensions. In the Schwarzschild case the spherical symmetry of the background metric makes it possible to separate the radial and angular

dependencies so that the equations simplify to a set of 1+1 dimensional wave equations for each spherical harmonic mode.

Following Moncrief, we begin by decomposing the perturbed metric in terms of Regge and Wheeler's spherical harmonic expansion. In this expansion the spatial part of the metric is represented by six radial functions for each angular mode (*i.e.* for each  $(l, m)$  pair)

$$\begin{aligned}
 h_{ij} = & c_1(\bar{r}) (\hat{e}_1)_{ij} + c_2(\bar{r}) (\hat{e}_2)_{ij} \\
 & + h_1(\bar{r}) (\hat{f}_1)_{ij} + \frac{1}{\alpha^2} H_2(\bar{r}) (\hat{f}_2)_{ij} + \bar{r}^2 K(\bar{r}) (\hat{f}_3)_{ij} + \bar{r}^2 G(\bar{r}) (\hat{f}_4)_{ij}.
 \end{aligned} \tag{2.48}$$

In this expression  $\alpha$  is just the Schwarzschild lapse function,

$$\alpha = \sqrt{1 - \frac{2M_{Sch}}{\bar{r}}}, \tag{2.49}$$

$c_1$  and  $c_2$  are functions of the usual Schwarzschild radius  $\bar{r}$  and  $t$  governing odd-parity perturbations,  $h_1$ ,  $h_2$ ,  $K$ , and  $G$  are functions of  $\bar{r}$  and  $t$  which govern even-parity perturbations, and the  $\hat{e}_i$  and  $\hat{f}_i$  are symmetric matrices which depend only on  $\theta$  and  $\phi$ ,

$$\hat{e}_1 = \begin{pmatrix} 0 & -\frac{1}{\sin\theta} \frac{dY_{lm}}{d\phi} & \sin\theta \frac{dY_{lm}}{d\theta} \\ \text{Sym} & 0 & 0 \\ \text{Sym} & 0 & 0 \end{pmatrix}$$

$$\begin{aligned}
\hat{e}_2 &= \begin{pmatrix} 0 & & 0 \\ 0 & \frac{1}{\sin\theta} \left[ \frac{d^2}{d\theta d\phi} - \cot\theta \frac{d}{d\phi} \right] Y_{lm} & \frac{1}{2} \left[ \frac{1}{\sin\theta} \frac{d^2}{d\theta^2} + \cos\theta \frac{d}{d\theta} - \sin\theta \frac{d^2}{d\theta^2} \right] Y_{lm} \\ 0 & \text{Sym} & - \left[ \sin\theta \frac{d^2}{d\theta d\phi} - \cos\theta \frac{d}{d\phi} \right] Y_{lm} \end{pmatrix} \\
\hat{f}_1 &= \begin{pmatrix} 0 & \frac{dY_{lm}}{d\theta} & \frac{dY_{lm}}{d\phi} \\ \text{Sym} & 0 & 0 \\ \text{Sym} & 0 & 0 \end{pmatrix} \\
\hat{f}_2 &= \begin{pmatrix} Y_{lm} & 0 & 0 \\ 0 & 0 & 0 \\ 0 & 0 & 0 \end{pmatrix} \\
\hat{f}_3 &= \begin{pmatrix} 0 & 0 & 0 \\ 0 & Y_{lm} & 0 \\ 0 & 0 & \sin^2\theta Y_{lm} \end{pmatrix} \\
\hat{f}_4 &= \begin{pmatrix} 0 & 0 & 0 \\ 0 & \frac{d^2 Y_{lm}}{d\theta^2} & \left[ \frac{d^2}{d\theta d\phi} - \cot\theta \frac{d}{d\phi} \right] Y_{lm} \\ 0 & \text{Sym} & \left[ \frac{d^2}{d\theta^2} + \sin\theta \cos\theta \frac{d}{d\theta} \right] Y_{lm} \end{pmatrix}.
\end{aligned} \tag{2.50}$$

The labels  $lm$  on all these quantities have been suppressed for simplicity. Gauge transformations of the perturbation will result in recombinations of the Regge-Wheeler coefficients within the sets of odd and even parity functions. To account for this without restricting the form of the perturbed metric, Moncrief has identified combinations of these coefficients which are not affected by linear gauge transformations. For odd-parity perturbations he finds that

$$Q_\times = 4 \frac{\alpha^2}{\bar{r}} \left[ c_1 + \frac{\bar{r}^2}{2} \frac{d}{d\bar{r}} \left( \frac{c_2}{\bar{r}^2} \right) \right] \tag{2.51}$$

is gauge invariant, and for even parity perturbations his results can be written as

$$Q_+ = \frac{4}{\Lambda} \left( 4\alpha^4 \bar{r} k_2 + 6\bar{r} k_1 \right) \quad (2.52)$$

where

$$\begin{aligned} k_1 &= K + \frac{\alpha^2}{\bar{r}} \left[ \bar{r}^2 \frac{d}{d\bar{r}} G - 2h_1 \right] \\ \text{and } k_2 &= \frac{1}{2\alpha^2} \left[ H_2 - K - \alpha \bar{r} \frac{d}{d\bar{r}} \left( \frac{K}{\alpha} \right) \right]. \end{aligned} \quad (2.53)$$

$\Lambda$  depends on the angular parameter  $l$ , for  $l = 2$  it has the value

$$\Lambda = 4 + 6 \frac{M_{Sch}}{\bar{r}} \quad (2.54)$$

where  $M_{Sch}$  is the background Schwarzschild mass. These gauge invariants match Moncrief's except for the the overall factor of 4 which has been included for consistency with the normalization used in previous perturbative studies.[17, 18] Again the  $lm$  indices are suppressed. In terms of these functions the subset of the linearized Einstein's equations which govern evolution simplify to.

$$\frac{d^2 Q_\times}{dt^2} - \frac{d^2 Q_\times}{dr^{*2}} = V_\times Q_\times \quad (2.55)$$

$$\frac{d^2 Q_+}{dt^2} - \frac{d^2 Q_+}{dr^{*2}} = V_+ Q_+ \quad (2.56)$$

where

$$\begin{aligned}
V_{\times} &= -\alpha^2 \left( \frac{l(l+1)}{\bar{r}^2} + \frac{6M_{Sch}}{\bar{r}^3} \right) \\
V_{+} &= \alpha^2 \left[ \frac{1}{\Lambda^2} \left( \frac{72M_{Sch}^3}{\bar{r}^5} - \frac{12M_{Sch}}{\bar{r}^3} (l-1)(l-2) \left( 1 - \frac{3M_{Sch}}{\bar{r}} \right) \right) \right. \\
&\quad \left. + \frac{(l-1)(l+2)l(l+1)}{\bar{r}^2 \Lambda} \right]. \tag{2.57}
\end{aligned}$$

These evolution equations apply to perturbations with  $l \geq 1$ . Perturbations with smaller  $l$  do not evolve. Rather,  $l = 0$  perturbations correspond to changes in the Schwarzschild mass and  $l = 1$  are related either to the ADM angular momentum, in the odd-parity case, or even parity displacement of the coordinate origin.

#### 2.4.2 Initial Values for $Q_{\times}$ and $Q_{+}$

To apply this formalism to our problem now is simple. We need only use our initial data derived in the last section to give specific initial values for Eq. 2.55 and Eq. 2.56 and then integrate. Moncrief's formalism tells us how to derive the initial values for  $Q_{\times}$  and  $Q_{+}$  from the initial metric perturbation with the background metric written in the usual Schwarzschild coordinates. The initial derivatives,  $\dot{Q}_{\times}$  and  $\dot{Q}_{+}$  are calculated similarly from the initial time derivative of the metric perturbation. In the last section we derived approximate two black hole initial data in the form of a conformal factor and extrinsic curvature. The conformal factor will determine the initial values of the Regge-Wheeler and Zerilli functions, and the extrinsic curvature will determine the initial derivatives.

By comparing Eq. 2.36 and Eq. 2.37 which give the approximate conformal factor with the Schwarzschild metric Eq. 2.41 it can be shown that the approximate initial metric perturbation is, in isotropic coordinates,

$$h_{ij} = \kappa_2 \psi_{sch}^3 \frac{M_{Sch}^3}{r^3} (3 \cos^2 \theta - 1) \begin{pmatrix} 1 & 0 & 0 \\ 0 & r^2 & 0 \\ 0 & 0 & r^2 \sin^2 \theta \end{pmatrix} \quad (2.58)$$

where  $\psi_{sch}$  is the conformal factor that puts the Schwarzschild metric in isotropic coordinates,

$$\psi_{sch} = 1 + \frac{M_{Sch}}{2r} = \frac{2}{1 + \alpha} \quad (2.59)$$

Making the transformation to the Schwarzschild radial coordinate,  $\bar{r}$ , by

$$r = \bar{r} \psi_{sch}^{-2} = \frac{\bar{r}}{4} (1 + \alpha)^2, \quad (2.60)$$

gives the desired form of the metric perturbation,

$$h_{ij} = \kappa_2 \psi_{sch}^5 \frac{M_{Sch}^3}{\bar{r}^3} (3 \cos \theta - 1) \begin{pmatrix} \alpha^{-2} & 0 & 0 \\ 0 & \bar{r}^2 & 0 \\ 0 & 0 & \bar{r}^2 \sin^2 \theta \end{pmatrix}. \quad (2.61)$$

This perturbation has purely ( $l = 2, m = 0$ ), even-parity angular dependence and its Regge-Wheeler coefficients are

$$K = H_2 = \sqrt{\frac{4\pi}{5}} \left(\frac{2}{1+\alpha}\right)^5 \frac{M_{Sch}^3}{\bar{r}^3} \quad (2.62)$$

with all other coefficients vanishing. Then we use Eq. 2.52 to calculate  $Q_+$  yielding

$$Q_+ = \sqrt{\frac{4\pi}{5}} \left( \frac{4}{4 + 6\frac{M_{Sch}}{\bar{r}}} \right) \left(\frac{2}{1+\alpha}\right)^5 \frac{M_{Sch}^3}{\bar{r}^2} (7 + 5\alpha). \quad (2.63)$$

We obtain the initial time derivatives of the Regge-Wheeler and Zerilli functions from the initial values of the extrinsic curvature. If we make the gauge choice that the shift vector is initially unperturbed and, hence, vanishes then the initial time derivative of the metric is given by the familiar relation

$$\dot{h}_{ij} = -2\alpha K_{ij}. \quad (2.64)$$

Here  $\alpha$  is still the unperturbed Schwarzschild lapse function and  $K_{ij}$  is the perturbation of the physical extrinsic curvature. In this case, of course, the background extrinsic curvature vanishes so that  $K_{ij}$  is just identical to the physical initial extrinsic curvature. Recall that the physical extrinsic curvature is related to the conformal extrinsic curvature by a multiple of the conformal factor, Eq. 2.3. Since  $\hat{K}_{ij}$  vanishes in the Schwarzschild limit, to get the linearized physical extrinsic curvature we use only the background



conformal factor,  $\psi_{sch}$ , with the result,

$$K_{ij} = \psi_{sch}^{-2} \hat{K}_{ij}. \quad (2.65)$$

Once  $\dot{h}_{ij}$  is calculated, the next step is to decompose the tensor into its components to obtain  $\dot{c}_1, \dot{c}_2, \dot{h}_1, \dot{H}_2, \dot{K}$ , and  $\dot{G}$ . Then we can use the time derivatives of Eq. 2.51 and Eq. 2.52 to calculate  $\dot{Q}_\times$  and  $\dot{Q}_+$ ,

$$\dot{Q}_\times = 4\frac{\alpha^2}{\bar{r}} \left[ \dot{c}_1 + \frac{\bar{r}^2}{2} \frac{d}{d\bar{r}} \left( \frac{\dot{c}_2}{\bar{r}^2} \right) \right] \quad (2.66)$$

$$\text{and } \dot{Q}_+ = \frac{4}{\Lambda} (4\alpha^4 \bar{r} \dot{k}_2 + 6\bar{r} \dot{k}_1) \quad (2.67)$$

where again

$$\begin{aligned} \dot{k}_1 &= \dot{K} + \frac{\alpha^2}{\bar{r}} \left[ \bar{r}^2 \frac{d}{d\bar{r}} \dot{G} - 2\dot{h}_1 \right] \\ \text{and } \dot{k}_2 &= \frac{1}{2\alpha^2} \left[ \dot{H}_2 - \dot{K} - \alpha \bar{r} \frac{d}{d\bar{r}} \left( \frac{\dot{K}}{\alpha} \right) \right]. \end{aligned} \quad (2.68)$$

Explicitly calculating the results from Eq. 2.28, we find an  $l = 2, m = 0$  odd-parity contribution for the cosmic screw,

$$\dot{Q}_\times = \sqrt{\frac{4\pi}{5}} \frac{4L}{\bar{r}^4} \frac{\alpha}{(1+\alpha)^2} (1+6\alpha-7\alpha^2) J_{||}. \quad (2.69)$$

The Zerilli function derivatives corresponding to the two components of linear momentum turn out to be exactly proportional to each other, but with different angular dependencies. The “boost” part has  $l = 2, m = 0$  even parity with,

$$\dot{Q}_+^{\text{Boost}} = -\frac{12 L \alpha}{\bar{r}^2 (2 + 3M_{Sch}/\bar{r})} \sqrt{\frac{4\pi}{5}} \left(4 + \frac{3M_{Sch}}{\bar{r}}\right) P_{\parallel} \quad (2.70)$$

and the off-axis part is  $l = 2, m = -1$  even parity with

$$\frac{1}{P_{\perp}} \dot{Q}_+^{\text{Off-Axis}} = \sqrt{\frac{3}{4}} \frac{1}{P_{\parallel}} \dot{Q}_+^{\text{Boost}}. \quad (2.71)$$

## 2.5 Results

Here we will examine the gravitational radiation emitted in the evolution of our close black hole data sets, the waveforms. We clarify what we will mean by “waveforms” in §2.5.1 and provide an explanation of how the radiation energy is calculated.

Of our black hole configurations, the most interesting case is that of boosted collisions with initial inward linear momentum. Unlike the other cases these collisions exhibit an interesting interaction between the part of the waveform which depends on the momentum and the part of the waveform which depends only on the separation which results in a surprising “dip” in the energy versus momentum curves. The distinction between the “momentum part” of the waveforms and the “Misner part” has a central role in our analysis. The linear dependence of our initial data on the momentum makes it possible to get a qualitative picture of what the results should look like even before completing the quantitative calculations. §2.5.2 gives an analysis of our expectations

from the numerical results. The boosted collision results are given in §2.5.3. In this case we have completed a comparison with fully non-linear numerical results[19] calculated by Steve Brandt and other researchers. The comparison with the non-linear calculation shows surprising agreement for large values of momentum. An explanation of this agreement described as “momentum dominance” is discussed in section §2.5.3 as well as some analysis of what ultimately causes disagreement in the large momentum cases. §2.5.4 and §2.5.5 give the linear theory results for cosmic screws and off-axis collisions.

### 2.5.1 Waveforms and Radiation Energy

We interpret waveforms in this case to mean the time development to the Regge-Wheeler or Zerilli function evaluated at some sufficiently far away point. This has the advantage over, for example, looking at some metric function that the Regge-Wheeler and Zerilli functions are invariant with respect to first-order coordinate transformations. It is also valuable to maintain the spherical harmonic decomposition since this is the most natural summary of the waveform’s angular dependence information anyway. Furthermore in our case we are only interested in the  $l = 2$  angular modes. To first order, only the  $l = 2$  are affected by the introduction of some initial extrinsic curvature. For a physical zero-dimensional summary of the radiation information we also consider the total radiation energy emitted during the course of the collision for a particular spherical harmonic mode.

We will use the symbol  $\psi$  for waveforms,

$$\psi(t) = Q_{\times}(r_0, t) \quad \text{or} \quad Q_{+}(r_0, t) \quad (2.72)$$

for even or odd parity waves, where  $r_0$  is some sufficiently far away radius and we continue to suppress the labels.

For the case of even parity, we have followed the conventions of Cunningham, Price and Moncrief[18] so we can directly apply their expression for the radiation energy. In our notation for the  $l = 2$  case this becomes

$$E = \frac{1}{384\pi} \int_0^\infty \dot{Q}_+^2 dt. \quad (2.73)$$

For the case of odd parity we have used different conventions from Cunningham, Price and Moncrief[17] and can not directly apply their result. Nevertheless we can adapt their derivation with the observation that

$$\dot{k}_2 \sim -2rQ_\times, \quad (2.74)$$

which applies in the radiation zone limit, should be used in place of their Eq. III-20. Following the rest of their calculation yields the  $l = 2$  result,

$$E = \frac{24}{16\pi} \int_0^\infty \dot{Q}_+^2 dt. \quad (2.75)$$

This agrees with the expression given by Abrahams and Price[11] after taking into account the additional normalization factor on their  $Q_\times$ . The odd parity waveforms in this normalization, commonly used in non-linear numerical calculations differ from ours by the additional factor

$$\sqrt{2 \frac{(l+2)!}{(l-2)!}} \rightarrow 4\sqrt{12} \quad (2.76)$$

for  $l = 2$ .

### 2.5.2 Results Evident Before Calculation

Because the evolution is linear the evolved Zerilli or Regge-Wheeler function can be decomposed into two parts, one which arises from the initial values of the function with vanishing initial derivatives and the other which arises from the initial time derivatives. By our construction of the initial data the “initial values” part comes directly from the conformal factor which is identical to that for the Misner data and is unmodified by the addition of momentum. We call this part the “Misner part”. Conversely, the other component depends linearly on the momentum parameters so we call it the “momentum part”. In this way the waveform is decomposed into parts of zeroth and first order in the momentum or angular momentum,

$$\psi = \psi_{Mis} + \psi_{Mom}. \quad (2.77)$$

The Misner part,  $\psi_{Mis}$  comes only with even parity and  $l = 2, m = 0$  angular dependence. The  $l = 2, m = 0$  waveform then will only be modified from its Misner form by the part of  $\psi_{Mom}$  with even parity and  $l = 2, m = 0$  angular dependence, which is obtained only in the boost case. The parts of  $\psi_{Mom}$  which come from the cosmic screw and off-axis momentum configurations have respectively  $l = 2, m = 0, odd$  and  $l = 2, m = -1, even$  dependence. These will not interfere with  $\psi_{Mom}$ , but have completely independent evolution.

For the boost case the expression for the radiation energy can be written as,

$$E = \frac{1}{384\pi} \left( \int_0^\infty \dot{\psi}_{Mis}^2 dt + 2 \int_0^\infty \dot{\psi}_{Mis} \dot{\psi}_{Mom}^2 dt + \int_0^\infty \dot{\psi}_{Mom}^2 dt \right) \quad (2.78)$$

If we consider the dependence of radiation energy on the initial inward linear momentum of each hole,  $P$ , taking into account that only  $\psi_{Mom}$  depends linearly  $P$ , it is clear that Eq. 2.78 is the equation for a parabola. The middle term represents the interference between  $\psi_{Mis}$  and  $\psi_{Mom}$ . Unlike the other two terms, the sign of the middle term will not be evident until we perform the evolution. If there is destructive interference between the two parts of the waveform then this term will be negative and the dip of the parabola will lie in the domain of positive  $P$ , and conversely for constructive interference.

A similar expression for the radiation energy from cosmic screw and off-axis type collision would also, of course, imply a quadratic dependence on the initial angular or linear momentum parameter but in these cases there is no possibility for interference and the parabola will be centered at zero momentum. If we were to perform calculations for the other momentum parameters mentioned in §2.3.1 we would similarly find no possibility for an interference term either with  $\psi_{Mis}$  or among any of the components of  $\psi_{Mom}$  that depend on the various parameters. Thus the general expression for  $E$  at constant separation in terms of all momentum parameters has no cross-terms and the only linear term is the interference term arising in the boost case as discussed above.

It is also interesting to consider the dependence of Eq. 2.78 on separation. To make the separation dependence explicit we can write

$$E = (\kappa_2)^2 C_{Mom,Mom} + \kappa_2 \frac{L}{M} P C_{Mom,Mis} + \left(\frac{L}{M}\right)^2 P^2 C_{Mis,Mis}, \quad (2.79)$$

where  $\kappa_2$  depends on  $\frac{L}{M}$  as discussed in §2.3.4.2. As we have considered it above, disregarding the separation dependence, the first term seems “largest” and the third term, proportional to  $P^2$  seems least significant. However, taking into consideration the extreme close limit behavior  $\kappa_2 \sim \mathcal{O}\left(\left(\frac{L}{M}\right)^3\right)$ , it is apparent that the third term is dominant and the first term is least significant unless  $P \leq \mathcal{O}\left(\left(\frac{L}{M}\right)^2\right)$ . Our arguments in the construction of the initial data allow us to consider the full range of  $P$  values up to at least  $\mathcal{O}\left(\frac{L}{M}\right)$ , over this range all three terms can be significant. A similar argument applies to the  $E$  dependence on the spin,  $J_{||}$ , and the off-axis momentum  $P_{\perp}$ .

### 2.5.3 Boosted Collisions

In Fig. 2.2 show the radiation waveforms resulting from the collision of close black holes with initially inward linear momentum, our “boost” case. As discussed in the last section, the manner of interference between the two parts of the waveform dictates whether the second term in Eq. 2.78 will have positive or negative sign and hence also whether the dip in the energy versus momentum curves will be on the side of inward or outward initial momentum. It is evident in the figure that the two parts of the waveform interfere destructively, thus we will have a dip in the domain of inward initial momentum. Filling in the values obtained from the numerical calculation Eq. 2.79 for

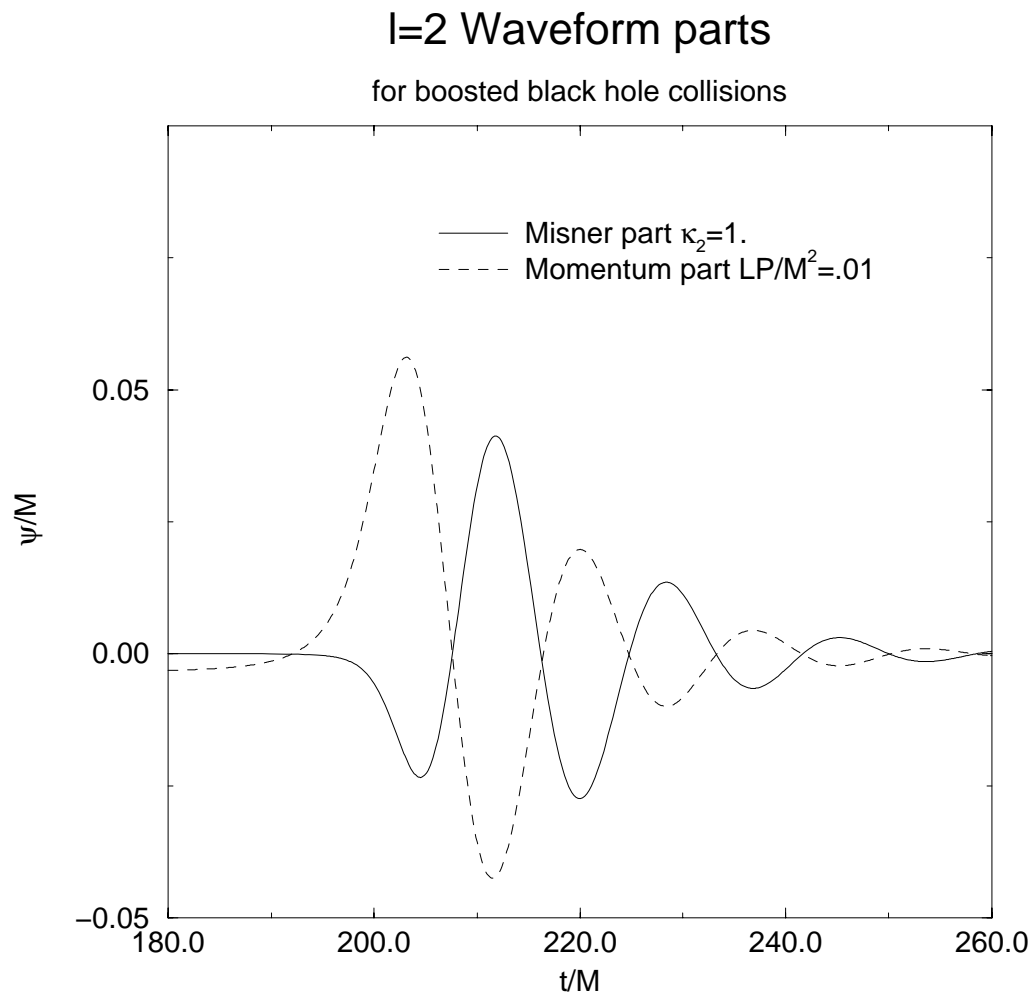


Fig. 2.2. This figure shows the shapes of the Misner waveform and the  $l = 2, m = 0, even$  boost waveform the destructive interference which leads to the dip in the energy curves is evident. These waveforms are evaluated at  $\bar{r} = 200M_{Sch}$ .



the energy as a function of separation and momentum gives a concise expression for the radiation energy predicted by the close-slow approximation,

$$\frac{E}{M} = 2.51 \times 10^{-2} (\kappa_2)^2 - 2.06 \times 10^{-2} \kappa_2 \frac{L}{M} \frac{P}{M} + 5.37 \times 10^{-3} \left(\frac{L}{M}\right)^2 \left(\frac{P}{M}\right)^2. \quad (2.80)$$

We will indicate separations by  $\mu_0$  which is related to  $\kappa_2$  and  $\frac{L}{M}$  as described in §2.3.4.2.

The curves of gravitational radiation energy as a function of initial inward momentum for two initial separations with  $\mu_0$  values of 0.7 and 1.5 are given in Fig. 2.3. The dip is plainly evident in the curves.

### 2.5.3.1 Comparison with Numerical Evolution

For the case of boosted black hole collisions, we have been able to compare with fully nonlinear numerical results calculated by researchers at the *Natioal Center for Supercomputer Applications*[19] Their calculations begin from initial data of the same family which we have approximated in above. The comparison of close approximation energies with those from the numerical calculation are shown in Fig. 2.3. There is excellent agreement between the numerical and linear results even at large values for the initial momentum. In logarithmic terms the worst error is at the largest momenta, but there is also some noticable error at the location of the dip. These features are discussed in more detail below. Fig. 2.4 shows that the linear and numerical results agree reasonably well in the details of the waveforms as well.

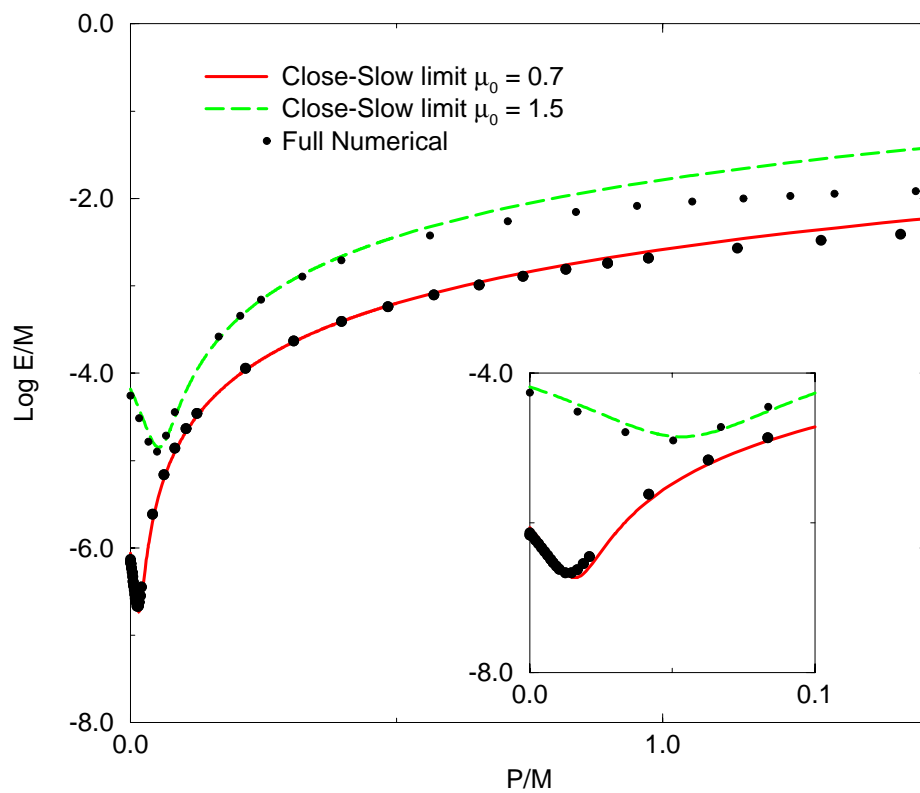


Fig. 2.3. Here we show the energy as a function of momentum for several choices of separation. The dip in energy arising from cancellation between the Misner and momentum parts of the waveform is clearly evident. The fully nonlinear numerical result is included for comparison. Reproduced from Ref. [19] with permission. Copyright ©1997 by the American Physical Society.

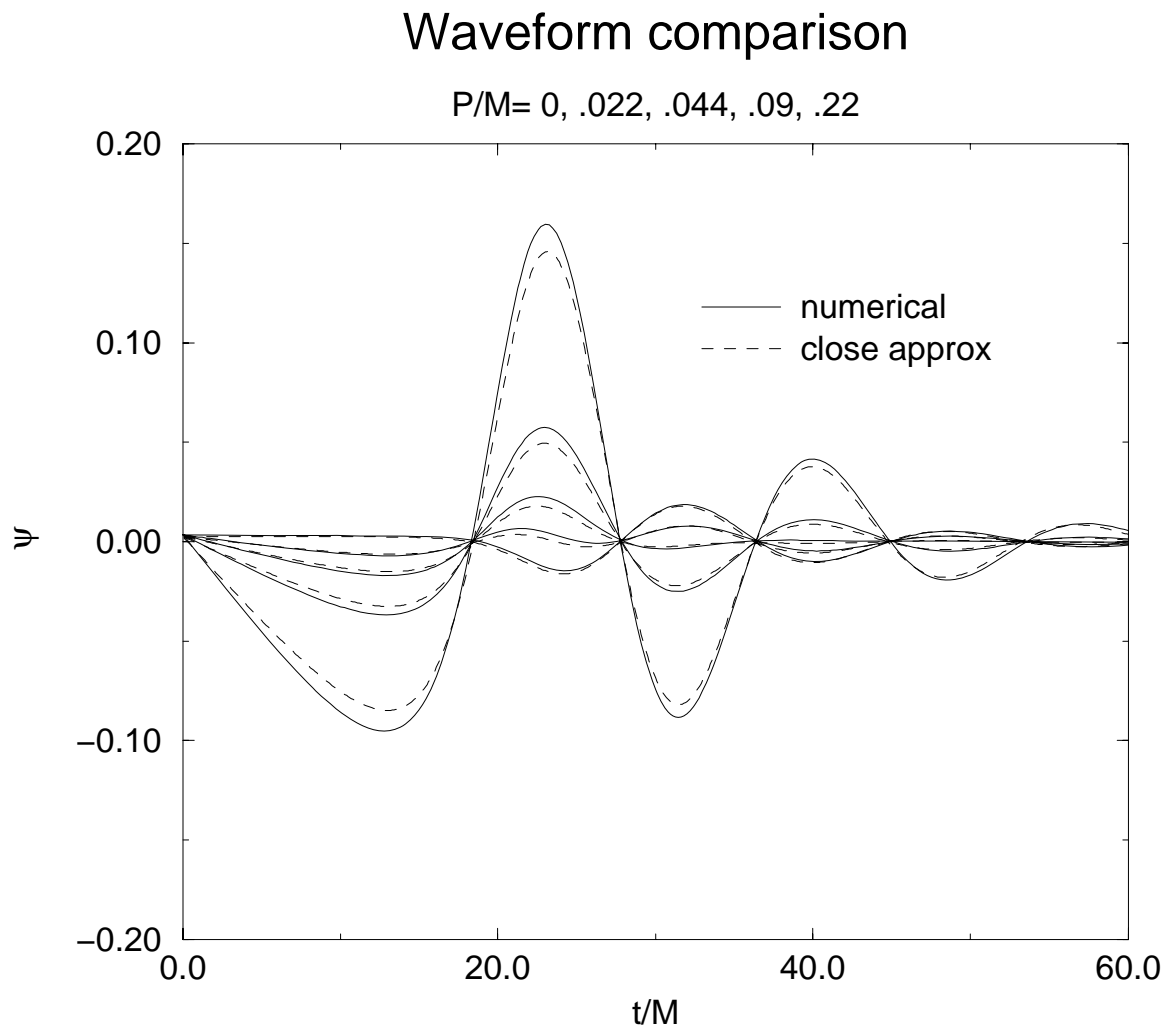


Fig. 2.4. These are waveform comparisons, evaluated at  $\bar{r} \sim 15M_{Sch}$  with  $\mu_0 = 1.0$  for several relatively small values of  $P/M$ . Note the agreement between the linear and nonlinear calculations.

### 2.5.3.2 Momentum Dominance

Notice in Fig. 2.3 that, after the dip, the agreement improves. In the dip itself linear calculation nearly cancels out leaving room for non-linear features to stand out. In the middle range the momentum is not extremely large but large enough so that the third term in the energy expression Eq. 2.78 dominates. Beyond this point Recall from the discussion in §2.5.2 that this term should begin to dominate once  $\frac{P}{M}$  becomes larger than  $(\frac{L}{M})^2$ . This transition from Misner part at  $P = 0$  to *momentum dominance* in the waveform at moderate values of momentum is illustrated in Fig. 2.5.

Where the momentum term dominates it can be said that the radiation response from perturbations of the extrinsic curvature is more significant than the response to the initial perturbation of the metric. The good middle-range agreement with the numerical calculation is an indication that corresponding exact space time is linearly dissipating the non-spherical features in the initial extrinsic curvature. In the energy curves, the location of dip is an indication of where the amount of radiation in response to the initial extrinsic curvature is overtaking the response from the initial metric perturbation. As is suggested by the two curves Fig. 2.3, this transition happens sooner in  $P$  for smaller separations. We expect the transition roughly near the parameter space curve where  $P = L^2/M$ .

Momentum dominance also helps to explain why the calculation agrees so well with the numerical calculation for large values of  $P/M$ . Recall that, regarding  $\frac{L}{M}$ , now as the basic perturbation parameter, we were required to take  $P/M \leq \frac{L}{M}$  only to control the source term in the Eq. 2.6 the Hamiltonian constraint. Considering what

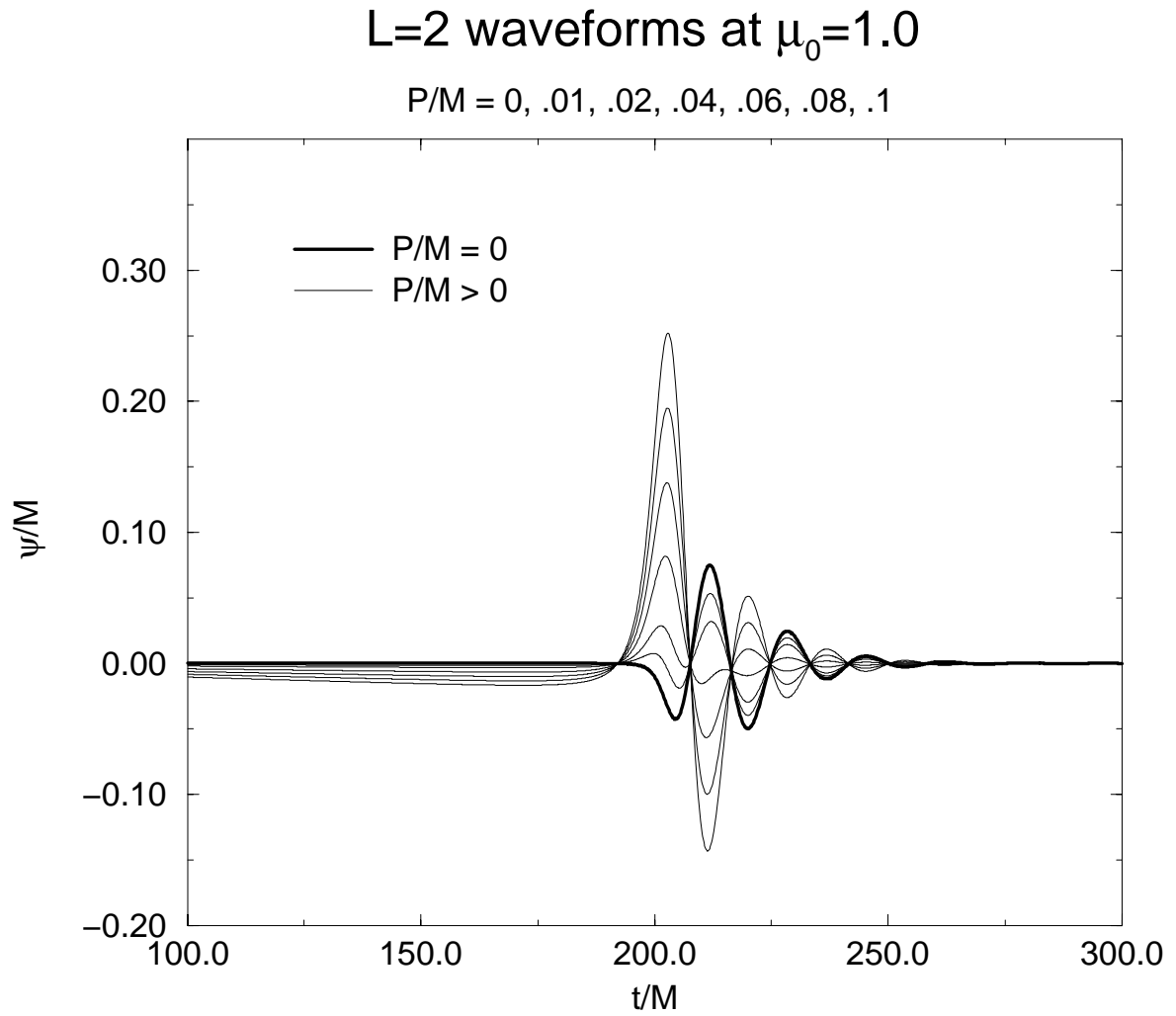


Fig. 2.5. This figure shows the inversion of the linear wave forms from boosted black hole collisions as the initial momentum is increased. The partial cancellation results in a dip in the radiation energy as the momentum increases. These waveforms have been evaluated at  $\bar{r} = 200M_{Sch}$ .

was just said above about the transition point to momentum dominance it is clear that for sufficiently close black holes the extrinsic curvature contributions to the waveform will already be dominant before the error made in solving the Hamiltonian becomes significant. While the Hamiltonian constraint is non-linear, the  $\psi^{-7}$  factor source term of the elliptic equation makes it unlikely that the  $l = 2$  part of the exact solution for the conformal factor would grow faster than  $P^2$ , therefore the momentum dominance should persist as long as the linear approximation for evolution is appropriate.

### 2.5.3.3 The Mass Scale Error for Large $P$

Does the disagreement with the numerical results for larger momenta imply significant non-linearities in evolution? We can approach this question by taking a more detailed look at the numerical waveforms. We can extract a “momentum part” from the numerical waveforms by subtracting out the  $P = 0$  waveform at a particular separation and dividing by  $P/M$ . Our analysis suggests that these momentum parts should be the same for each numerical run at a particular separation if the evolution is effectively linear. However, for large enough momentum our assumption that the mass of the initial slice is equivalent to the Misner mass will break down and we can then expect disagreement among our numerical momentum parts by an overall scale factor related to  $\chi$  from §2.3.4.1. Tracing the effect of the assumption that  $\chi = 1$  through our calculations leads to the result that if the true initial mass increases by a factor of  $\chi$ , our present momentum part waveforms will be found to be a factor of  $\chi$  too large. On comparing the numerical waveforms, then, it would not be surprising to find an overall downscaling with increasing  $P/M$  which is a consequence not of nonlinear dynamics but

of nonlinear scaling in the initial data. There is no reason to expect nonlinear dynamics to produce an overall rescaling of the waveform, but rather some change in the shape of the waveform.

The actual comparison of the numerical momentum parts does show a rescaling error for larger values of  $P/M$ . Assuming that this difference represents  $\chi$  we should then compare the waveforms, scaled to match, to look for nonlinear effects. The result is shown in Fig. 2.6. The excellent agreement of the waveforms suggests that the dynamics is linear at separation  $\mu_0 = 1.0$  and over the range of momenta at least up to  $P = M$ . The discrepancies appearing at the late ends of the waveforms have more the character of numerical error than what would be expected from nonlinear dynamics.

#### 2.5.4 The Cosmic Screw

The cosmic screw configuration results in an  $l = 2, m = o$  odd-parity momentum part waveform shown in Fig. 2.7. As explained in §2.5.2 there is no possibility in this case for any interference with the even parity Misner part of the waveform so there is no dip in the energy versus  $J_{||}$  curves are simply parabolas centered at  $J_{||} = 0$ . The radiation energy curves are shown in Fig. 2.8. As with the boost case the energy quickly grows orders of magnitude larger than that for Misner data. And again there is momentum dominance in the waveforms already at small values of spin evident in the curves wherever the energy is more than twice the  $J_{||} = 0$  value.

Without exact numerical values for the mass we can only provide an estimate here of the effect that our  $\chi = 1$  assumption about the mass has in this case. We have performed two types of estimate. For the  $\mu_0 = 1.0$  curve we have estimated the mass

## Momentum Part of NCSA Waveforms

19 waveforms with P/M optimized to match, range (P/M=.02 to 1.4)

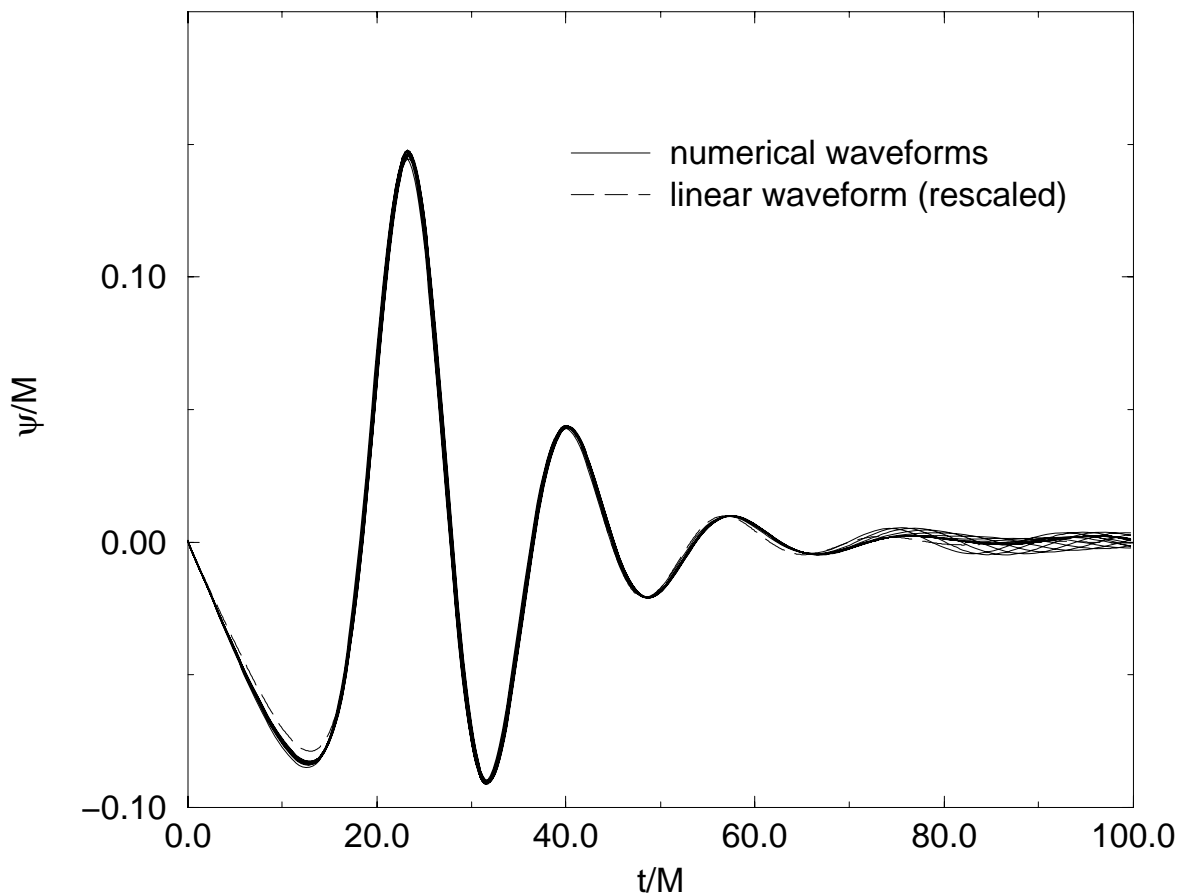


Fig. 2.6. Here we show a superposition of 19 “momentum parts” from the numerical waveforms rescaled to allow for the momentum dependence of the initial mass. The excellent match suggests linear dynamics despite the disagreement between the linear and numerical energies at large momenta. A linear momentum part is also shown for comparison. The wave forms were evaluated at  $\bar{r} \sim 15M_{Sch}$ .



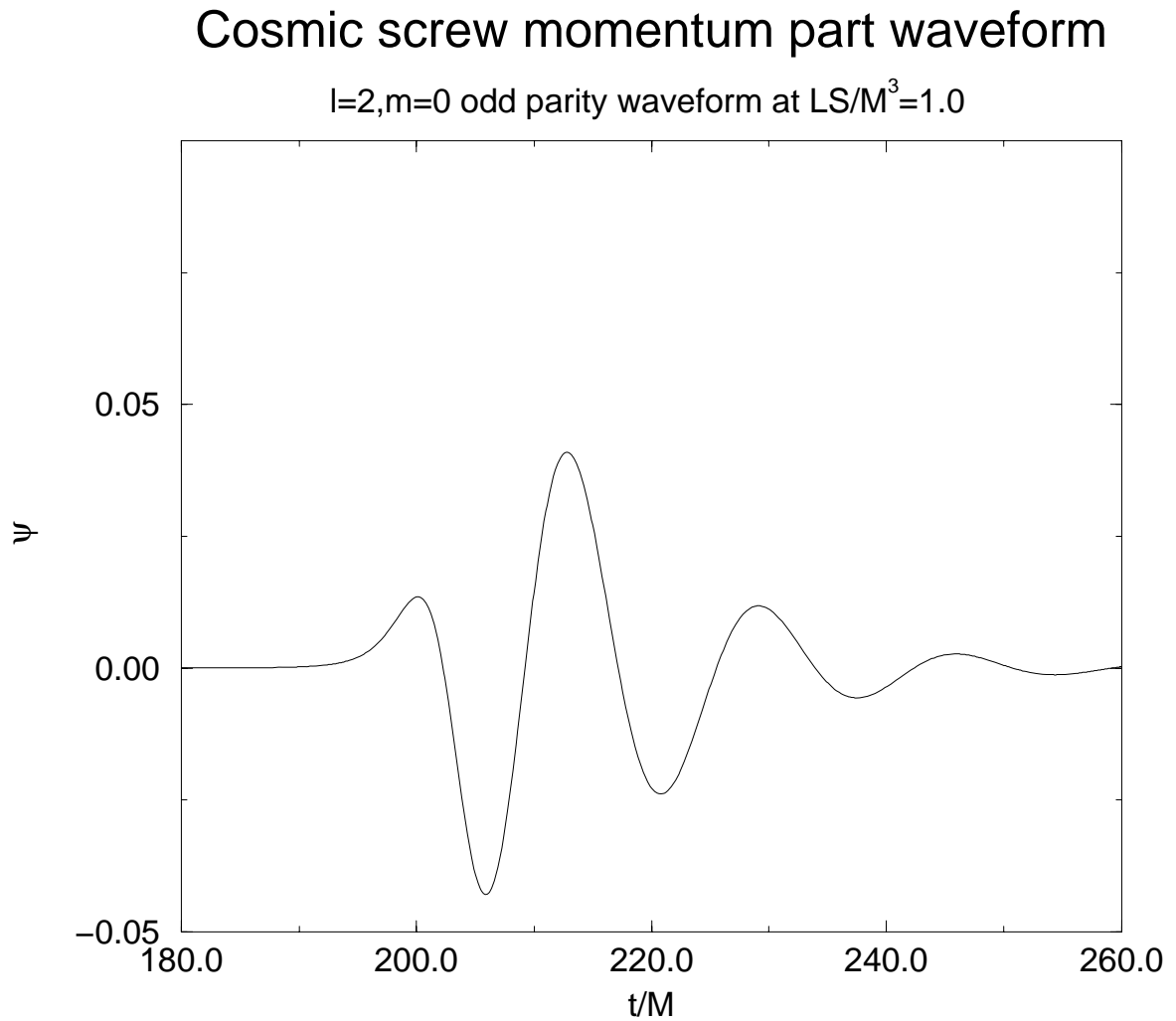


Fig. 2.7. The cosmic screw  $l = 2, m = 0$  odd-parity momentum part waveform evaluated at  $\bar{r} = 200M_{Sch}$ .

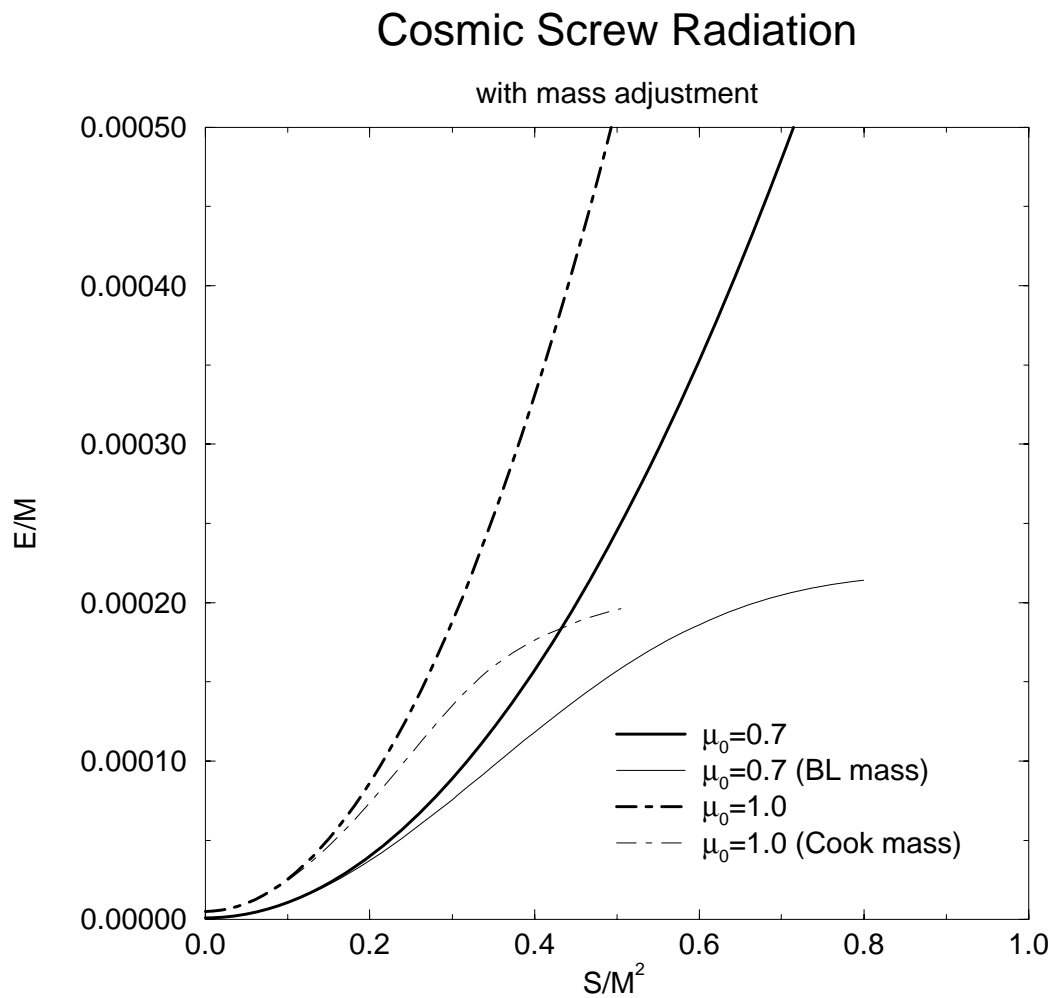


Fig. 2.8. The radiation energy curves for the cosmic screw configuration with estimated corrections to account for the mass under-estimate in our treatment.

ratio based on the results of Greg Cook's studies of the Bowen-York initial data sets.[9] For the  $\mu_0$  curve we have estimated the correction based on numerically calculated mass ratios for data with Brill-Lindquist type boundary conditions, not strictly applicable to our symmetrized boundary condition data, but probably good enough for a general idea. The effect is qualitatively the same in both cases, the total radiation tops out at a small value, around .02% of the mass.

### 2.5.5 Off-Axis

The last case we consider here is the off-axis collision. Recall that the off-axis  $\dot{Q}_+$  initial value curve is identical to that for the boosted black hole collisions except that it comes with  $l = 2, m = -1$  angular dependence instead of  $l = 2, m = 0$  dependence. Since the Zerilli equation does not depend on the angular label  $m$ , the shape of the off-axis momentum part waveform will be identical to momentum part waveform of the boost case so we do not show it here.

The off-axis configuration data contains non-vanishing net angular momentum of  $J = LP_{\perp}$ . We expect the final product of the collision to be a Kerr black hole so Schwarzschild perturbation theory is only appropriate when  $J$  is small enough that the angular momentum does not have a significant effect on the evolution. If we consider the radiation energy as a function of  $J$ , we again find a parabolic dependence, but with the slight difference from the dependencies we have considered so far that the  $J$  dependence does not depend on the separation.

In Fig. 2.9 we show a comparison of energy dependence on orbital and angular momentum to illustrate this difference. Momentum dominance is again evident, but

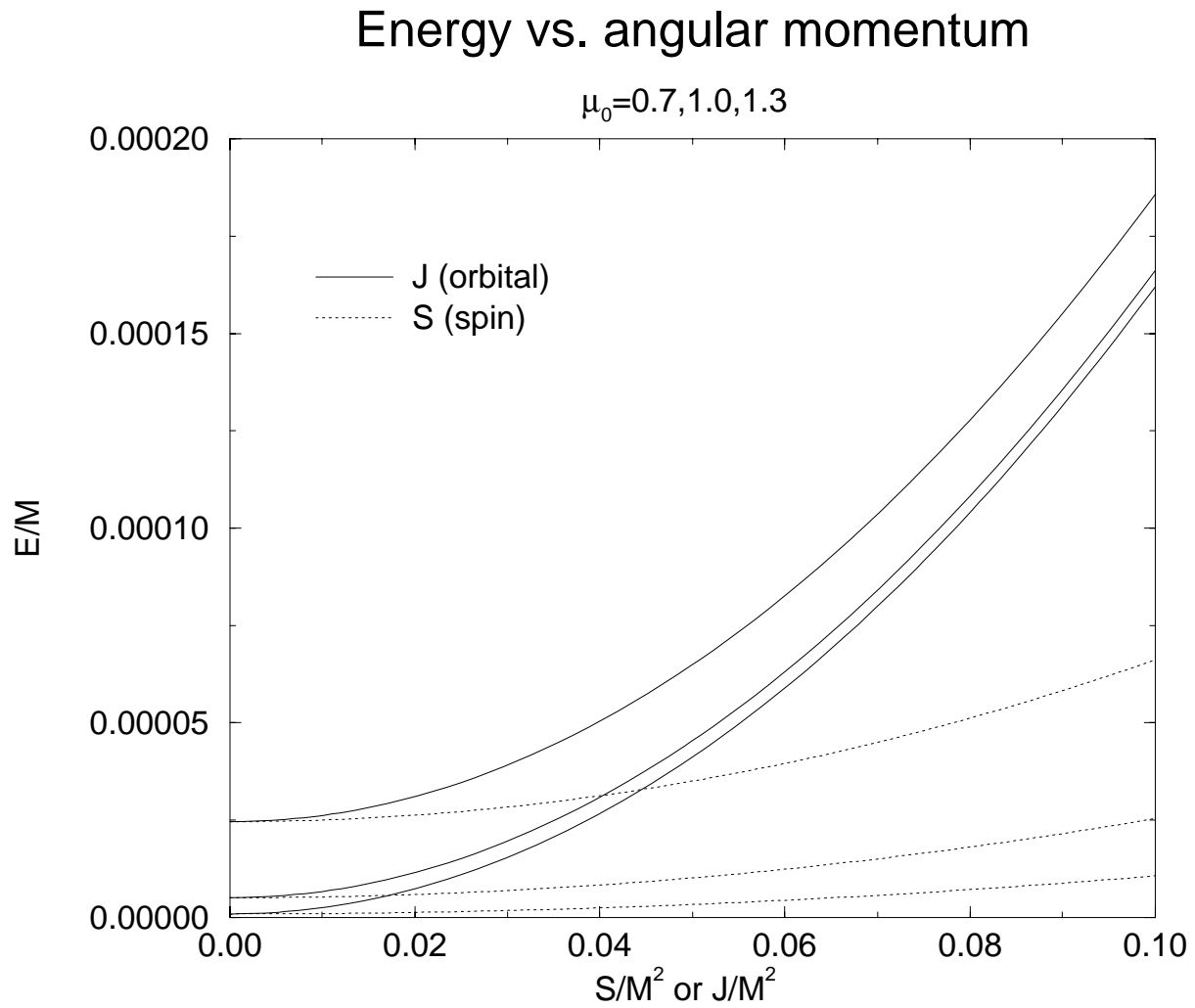


Fig. 2.9. Here we show a comparison of the radiation energy dependence on spin and orbital angular momentum. A notable feature is that the dependence on  $J$  is independent of the separation.

there is no point in considering the mass error because it would not be appropriate to allow  $J$  to become significant compared to the initial mass.

Since we have considered two components of the initial linear momentum we can look at the effect of allowing the angle of the initial momentum to vary. Fig. 2.10 shows the radiation versus  $J$  curves at various angles for the initial momentum away from the inward direction. For the cases where there is some initial inward component there is an initial dip as found in the boosted black hole collisions. Another interesting feature in the figure is the regrouping of the curves as the momentum increases. This exchange is a consequence of the transition to momentum dominance as the angular momentum increases. At low angular momentum, the initial separation is the most significant. Farther on the angle is most important, with the more inward angles indicating the most energy. Recall that the  $J^2$  coefficient in the energy curves does not depend on separation, thus in the momentum dominated region the more inward angle results only in the addition of inward momentum and should increase the radiation. In the momentum dominated domain this coefficient approaches an angular dependence proportional to  $(\csc^2 \theta - 1/4)$  which determines the constant factor energy differences seen on the right side of Fig. 2.10.

## 2.6 Discussion

For the case of boosted black holes, where numerical results were available for comparison, the close-slow approximation has made it possible to explain several features of the results which were otherwise mysterious. The energy dip, for example, was a

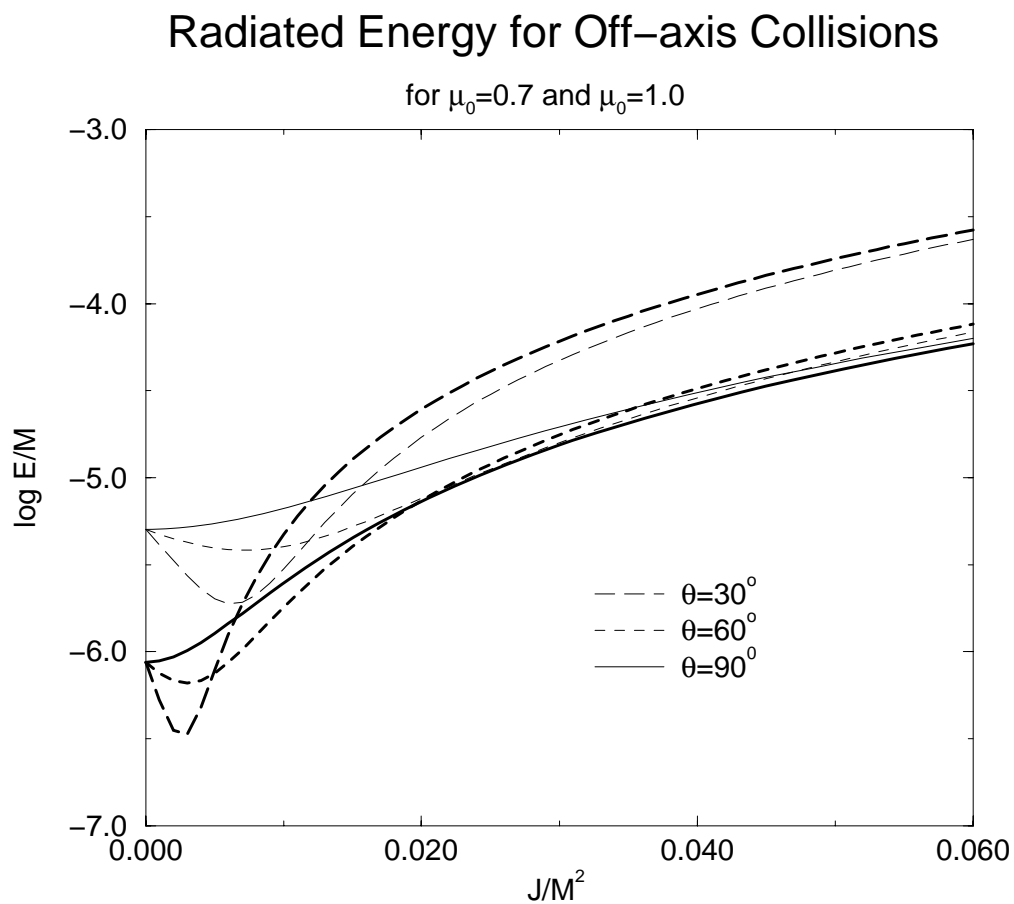


Fig. 2.10. Here we show the radiation energy dependence on the initial angle of the linear momentum away from the inward direction. The inward component results in a dip at low values of  $J$ . The crossing-over of the curves is a consequence of the transition to momentum dominance.

surprise to the researchers who performed the numerical calculation, and they suspected an error in their calculation until they learned of the close-slow results.

For the boosted black hole collisions, other researchers have since calculated the second order Schwarzschild perturbations for similar initial data with Boyer-Lindquist type boundary conditions. The results support what is seen in the comparison with the numerical calculation. The second order corrections are more significant in the dip area of the energy curves, tending to correct the first order values. The importance of using the exactly calculated mass was better appreciated after these results so there is no analogy with high momentum mass underestimate in the second order calculations.

## Chapter 3

# Two-Phase Evolution

<sup>1</sup> In this chapter we apply some of the results for boosted black hole collision to test the robustness of a scheme described by Abrahams and Cook[21] for using the evolution results from initially nearby black hole data to estimate radiation energies expected from the collision of initially distant black holes.

### 3.1 Introduction

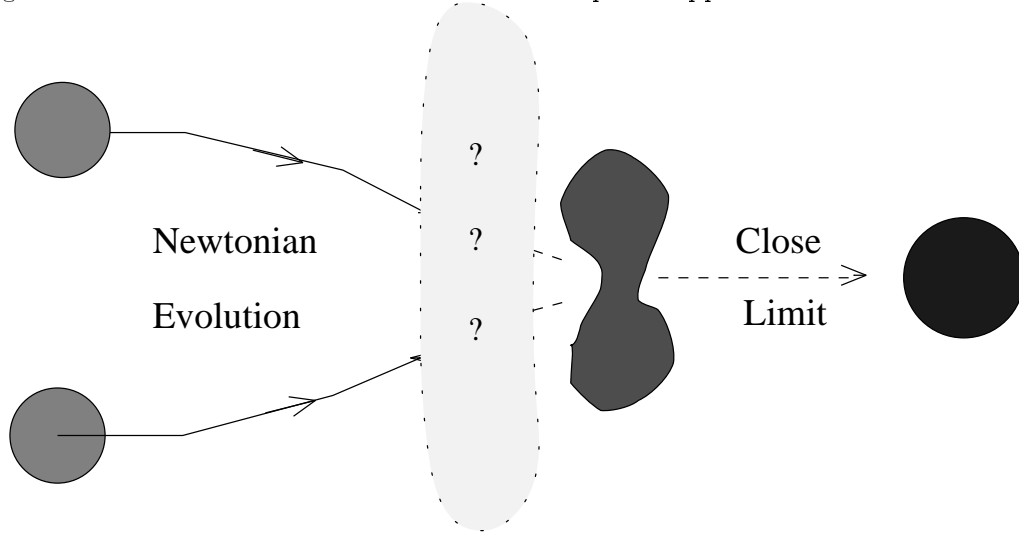
In the last chapter we applied the close-slow approximation to provide a check of numerical calculations and to provide a qualitative interpretation of some features of the collisions apparent in both the linear and numerical results. The relevance of the black hole collision problem as a source of detectable gravitational radiation invites an attempt to make use of close-limit results directly in this context. As we have discussed, for extremely close black holes we can treat the binary system as a linear perturbation of a single Schwarzschild black hole. This approximation is naturally expected to work well for evolution from initial data in which the two initial black holes are sufficiently close to be well inside a common horizon, but for the cases studied so far the results have shown good agreement with the numerical calculations even to separations where no common

---

<sup>1</sup>The material in this chapter is reproduced with permission and some minor reworking from Ref. [20]. Copyright ©1997 by IOP Publishing Ltd. For more information see their webpage, <http://www.iop.org/Journals/cq>.



Fig. 3.1. A cartoon illustration of how the two-phase approximation is constructed.



horizon exists.[19, 22] At the other extreme, if the black holes are far apart and moving slowly we might apply the Newtonian approximation, whereby the holes are treated simply as point particles moving in a flat background. Clearly, we can never understand the later and most important features of the collapse in only this far-limit. On the other hand, Fig. 3.1 schematically depicts the picture which emerges upon considering these approximations together. In a “realistic” head on black hole collision the black holes are initially well-separated as is indicated on the left side of the figure. For this part of the in-fall we can treat the holes as Newtonian point particles. In the subsequent evolution the black holes grow closer and their interaction grows stronger until the two holes merge into a single distorted black hole. This black hole radiates away its distortions, ultimately leaving a Schwarzschild black hole as the outcome. Between the Newtonian region and the region where the close-limit approximation applies there is a complicated transition

period which can only be understood by the exact numerical evolution. However we may note that at least for axisymmetric collisions nearly all of the radiation resulting from the collision is released in the final moments of collapse, when the black holes have already merged and the close-limit approximation works well.[19] One is then led to wonder if the essential characteristics of the radiation can be captured by stretching the range of the Newtonian and close-limit approximations until they meet to construct a two-phase approximation. If we restrict consideration to the total energy of the radiation generated by the collapse, might we achieve a good estimate of this radiation by using Newtonian mechanics to evolve the system of black holes until they are on the verge of coalescence, and subsequently evolving from this point using the close-limit approximation?

Abrahams and Cook first performed such a calculation in their study of black holes with initial inward momentum.[21] They applied the close-limit approximation to nearby black holes with just enough inward momentum to guarantee that they share a common apparent horizon in the initial data reasoning that the horizon formation point was an identifiable marker which roughly indicated the greatest separation at which the close-limit calculation would be successful. Then, they compared their results with those of the “exact” numerical calculation for the case of initially stationary black holes released from such a separation that Newtonian in-fall would provide the specified momentum at the moment of apparent horizon formation. The result was excellent agreement with the numerical calculation.

The Abrahams-Cook calculation seems to demonstrate the effectiveness of two-phase approximate evolution for treating initially distant black hole collisions. However, let us suppose the numerical result didn’t exist. Could we then claim that the two phase

approximation was generating a plausible estimate of the radiation? This is an important question because the close-limit approximation is currently being applied to problems which have not yet been solved numerically. The critical question in determining the usefulness of the two-phase approximation is whether the result is sensitive to how the Newtonian first phase is joined to the close limit second phase. For collapse from large separations, we know that the close-limit approximation will wildly overestimate the radiation. Similarly, we do not expect a reasonable result if we allow the Newtonian phase of the evolution to proceed too far. Unfortunately, we are left to choose the point between these extremes where we will switch from one type of evolution to the next. Thus it may turn out that our result will be strongly dependent on when we choose to make the transition. Our method is not useful if our uncertainty about the transition prevents us from making a sufficiently precise estimate of the radiation. Alternatively, if our prediction for the radiation were very insensitive to our choice of transition, then for a wide range of choices of transition, we would find only a narrow range of energy predictions. Then it would be compelling, though not rigorously justified, to infer that the correct result lies in that range. The goal of the work reported here is to determine whether there is such a narrow range of energies resulting from a wide class of transition choices, or whether the success of the Abrahams-Cook calculation was the result of a fortuitous choice of a Newtonian to close-limit transition at the point of apparent horizon formation.

### 3.2 Calculation

Our method is straightforward. We repeat the Abrahams-Cook calculation[21] varying the point along the in-fall trajectory at which Newtonian evolution ends and the close-limit evolution begins in order to see how strongly the result depends on this choice. A quick Newtonian-physics calculation shows that for equal mass particles colliding head-on,

$$\left(\frac{l}{m}\right)_0 = \frac{l/m}{1 - 8(P/m)^2(l/m)}, \quad (3.1)$$

where  $(l/m)_0$  is the initial separation from which the particles (black holes) are released at rest,  $l/m$  is the separation at some later point, and  $P/m$  is the magnitude of each hole's momentum at that point. All quantities are scaled by  $m$ , the combined bare mass of the black holes. The relation above defines a curve in the  $l$ - $P$  parameter space, the Newtonian trajectory of a system of in-falling particles. Thus, we have described the Newtonian phase of the evolution. At some point when the black holes are close, we will halt the Newtonian evolution and begin close-limit evolution.

In principle, at this transition we will switch from a description of the two black holes as a system of particles to a field-theoretic description, where the fields obey an approximate form of Einstein's equations. This requires us to specify values for the metric and its time-derivative on the initial time-slice in terms of the parameters  $l/m$  and  $p/m$  which have resulted from the Newtonian particle calculation. In principle there is no unique way make this specification; we must interpret the meaning of the particle parameters in the context of initial field configuration. In our case, to find the radiation, we will be using the results of the "close-slow" approximation which has been shown

to agree well with the numerical results for a broad range of initial momenta when the black holes are nearly close enough to have coalesced.[19] Implicitly, then, we will use the same description of the initial data as has been used in the close-slow calculation wherein the data are specified according to an approximation of the procedure developed by Bowen and York [8] and numerically solved for a wide variety of initial configurations by Cook.[9, 10] In this formalism, the initial slice is assumed to be conformally flat with traceless extrinsic curvature. A particular family of solutions for the extrinsic curvature, labeled by  $P$ , is chosen, and an elliptic boundary value problem determines the initial metric. After this, we must still interpret the quantities  $l$  and  $m$  as they will be realized for strongly interacting black holes. While it is natural to take  $l$  to be the proper separation between the minimum area throats associated with each black hole, there are several inequivalent ways to interpret the bare mass  $m$ . We choose to define the bare mass of each black hole as the mass associated with the area of its throat as is described in Ref. [10].

In practice, the second part of the evolution has already been solved. The results of the close-slow calculation for the energy radiated during the collision are summarized in Eq. 2.80. There all quantities are scaled by  $M$ , the ADM mass of the spatial slice. This equation gives us the total radiation directly in terms of  $\mu_0$  and  $P/M$ .

However, to use the above result we need know  $\mu_0$  and  $P/M$  in terms of the parameters  $l/m$  and  $P/m$ . Unfortunately, it is not natural in the conformal formalism to calculate the initial data directly from  $l/m$  and  $P/m$  as we interpret them here. Only after calculating the initial data sets in detail in terms of  $\mu_0$  and  $P$ , and then calculating the values of  $l$ ,  $m$  and  $M$  can we ascertain their relationship among these

parameters. Fortunately Cook[9] has performed a large number of such calculations generating tables of  $l$ ,  $m$  and  $M$  in terms of  $\mu_0$  and  $P$  for many cases covering the range of the parameter space with which we are interested. Instead of repeating these calculations, we find that we are able to get a sufficient estimate of  $\mu_0$  and  $P/M$  in terms of  $l/m$  and  $P/m$  by interpolation from Cook's results. Thus, we can apply the two-phase approximation to the evolution of distantly in-falling black holes without really doing any new calculations. Newtonian methods give us a concise equation for the first phase of evolution, the close-slow approximation gives us an equation for the second phase, and the translation between the two methods is accomplished by interpolation from existing studies of axisymmetric initial data.

### 3.3 Results

We seek to determine the sensitivity of the two-phase approximation result for the total radiation on the choice of transition. In Fig. 3.2 we plot this dependence for several different values of initial separation. The horizontal axis indicates the separation at which we make the transition from Newtonian to close-limit evolution. For example, the curve labeled " $\mu_0 = 2.5$ " shows that for holes released from rest at a separation of  $l \sim 5.5M$  the two-phase technique will find a minimum amount of radiation when the transition is made at  $l = 3.5m$ . The excellent agreement with the numerical results initially discovered by Abrahams and Cook was for the choice that the transition occurs at the point where the two black holes are just close enough to share a common apparent horizon. The energies at the horizon formation line indicated in the figure thus correspond to the Abrahams-Cook calculation. Note that for large initial separations, the total radiated

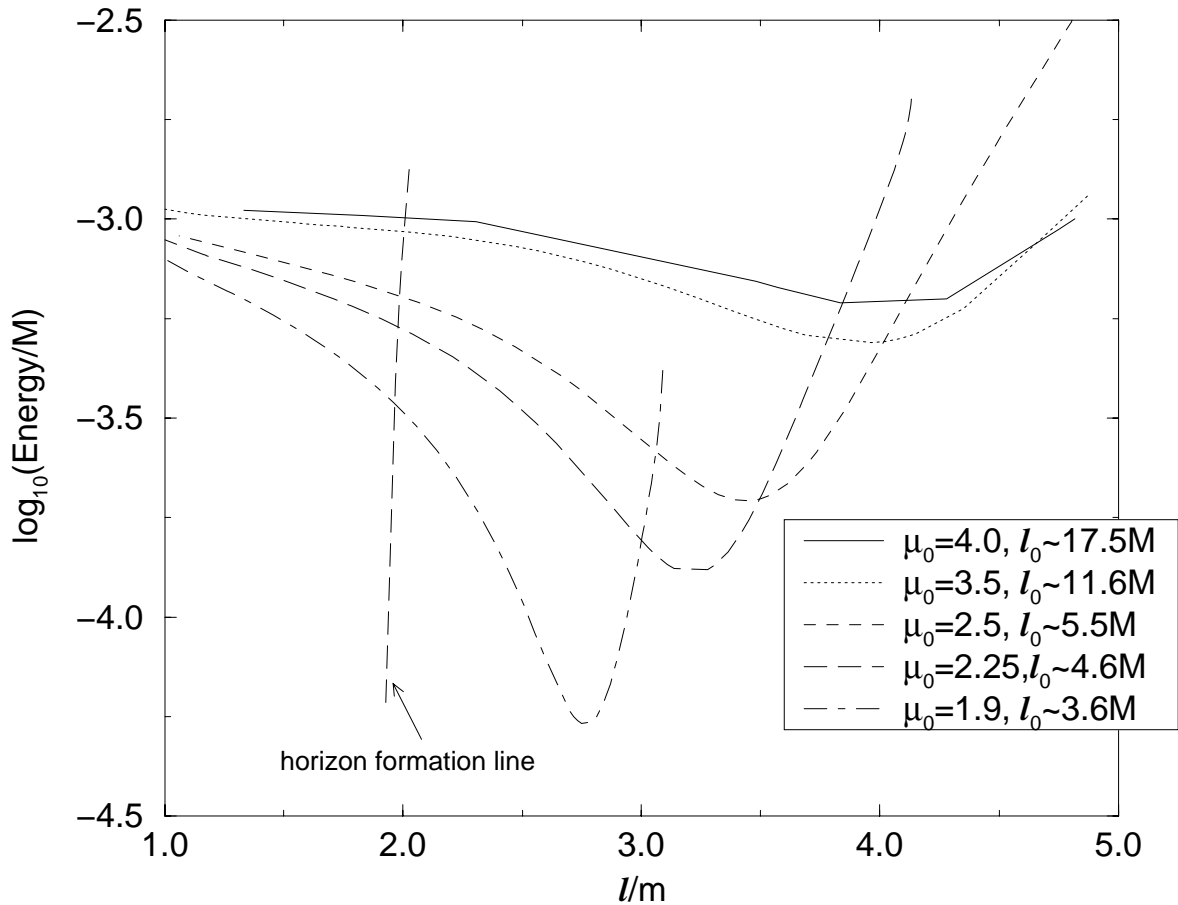


Fig. 3.2. Here we see that the amount of radiated energy is not sensitive to the choice of transition. The horizontal axis indicates the separation at which we switch from Newtonian to close-limit evolution. The curves show results for the radiation according to the two-phase approximation for collisions of black holes released from several different initial separations,  $\mu_0$ . It is evident that for holes released from significant initial distances the radiation result is not sensitive to the choice of transition as long as the transition is made somewhere in the vicinity of the separation at which a horizon first forms.

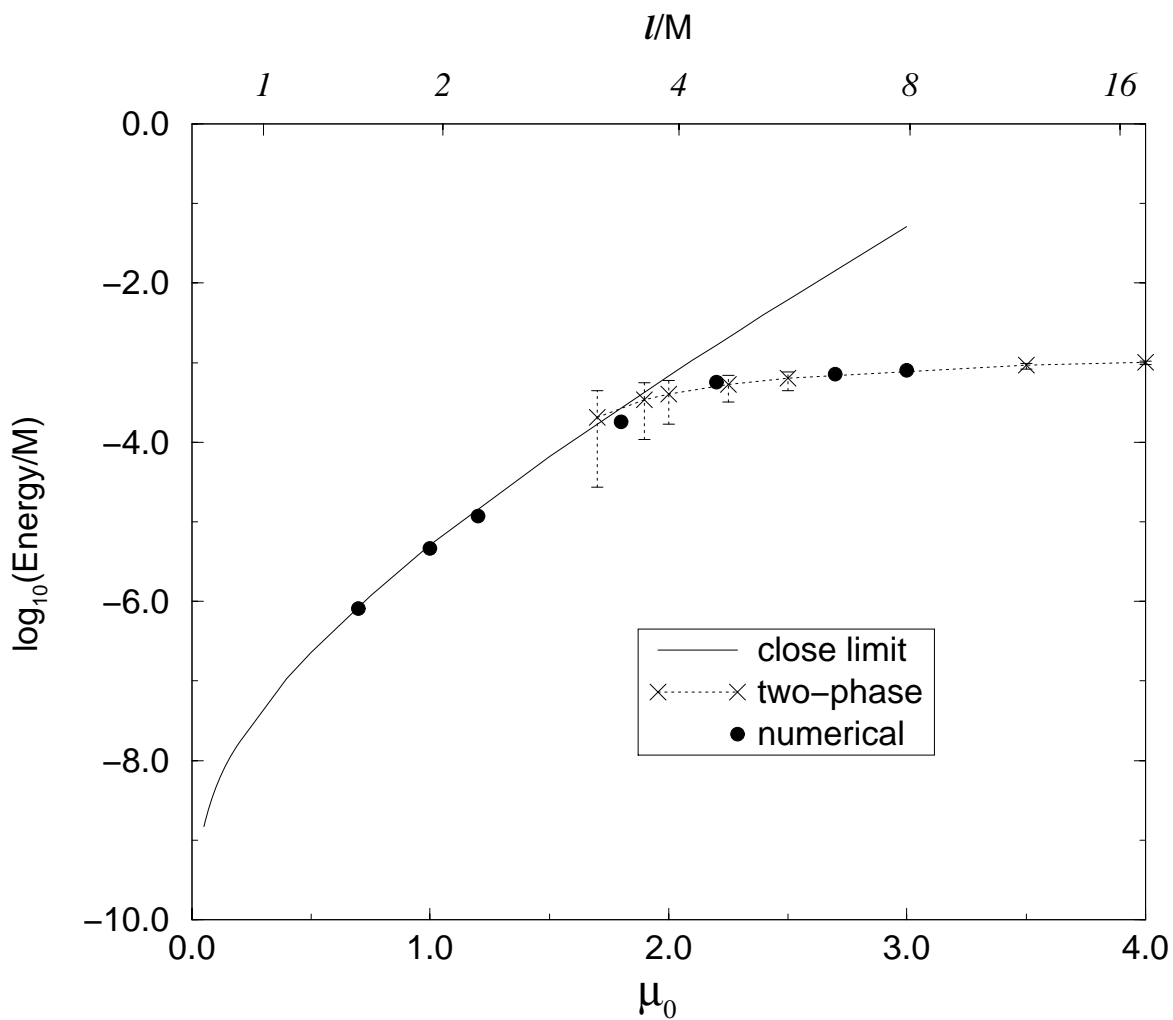


Fig. 3.3. This plot shows the excellent agreement of the two-phase approximation with the numerical result. The error estimates shown with the two-phase data are based on our analysis of the sensitivity of these results to the choice of separation at which we switch methods of evolution.



energy does not depend significantly on the choice of transition point in the vicinity of the horizon formation line. If the initial separation is greater than  $\mu_0 \sim 3.5$  is then even choosing to start the close-limit phase when the black holes are more than twice as far apart only changes the resulting radiation by less than a factor of two. As the initial separation becomes much closer the sensitivity begins to increase. This is not surprising since for initially close black holes there is essentially no stage of the evolution where the Newtonian particle method is appropriate. Fig. 3.3 shows a comparison of the two-phase approximation with the Pullin-Price close-limit result [6] and the result of the numerical calculation.[23] The error bars on the two-phase approximation result indicate the range of energies obtained if we allow the evolution transition to occur at any proper separation within  $\frac{1}{2}m$  of the apparent horizon formation point. As Abrahams and Cook have shown previously[21], there is excellent agreement with the numerical results. We conclude that the Abrahams-Cook approximate result for the radiation generated by in-fall from large initial separation is insensitive to the choice of transition from Newtonian to close-limit evolution. Together with the fact that the results for the radiation agree well with the numerical calculation, this suggests that the the two-phase approximation method may possibly be useful as a method for estimating the radiation generated in other types of black hole collisions.

## Chapter 4

### Initial Data for Kerr Perturbations

From an astrophysical point of view the most interesting configuration for a black hole collision is unlike the head-on collisions we have studied so far. We expect typical black hole coalescence to be the end stage of a slow inspiral process. We reasonably expect that, unlike Schwarzschild black holes, final black holes resulting from such collisions will have considerable angular momentum. The obvious extension of Schwarzschild perturbation work appropriate for this kind of problem is generalize to perturbations of Kerr black holes. Again the general theory of such perturbations has long ago been worked out.[24] And, although the resulting linearized evolution equations are not as simple as in the case of Schwarzschild perturbations, the numerical difficulties have been solved, and codes have been available for a few years now to apply to Kerr perturbation studies.[25] Still, no such black hole collision studies have been completed until very recently[26]. The trouble has been to provide suitable initial data for such calculations. This problem has been manifest in two ways. The lesser problem is the technical matter of specifying the initial values and initial derivatives of the Kerr perturbation function,  $\Psi_4$ , from conventional initial data given as an initial 3-metric and extrinsic curvature. This is discussed in the first section below. The more serious problem is to specify any meaningful initial data to represent close black holes which has Kerr data, with

non-trivial angular momentum, as a close limit. In part §4.2 we take some initial steps toward a new approach to specifying black hole initial data which has a Kerr close limit.

#### 4.1 Calculating $\Psi_4$

Before we can take advantage of techniques for evolving Kerr perturbations we must determine initial values of the Teukolsky function which correspond to an astrophysically interesting initial geometry. The problem of constructing black hole initial data in the form of a metric and extrinsic curvature has been studied extensively. Bowen and York type initial values have been widely applied in collision studies where conformal flatness is not a severe limitation. For the case of Kerr perturbations these data are not directly applicable because we are not aware of a conformally flat slicing of the Kerr geometry. The matter of determining an appropriate binary black hole initial geometry for Kerr perturbations is an interesting problem which is considered in §4.2. Here we will only address the much smaller problem of determining how to calculate the Teukolsky function on a perturbed slice of Kerr from the intrinsic metric on the slice and its extrinsic curvature.

We present a simple exposition of how to calculate the Teukolsky function on a spacelike slice from linear perturbations of the extrinsic curvature  $K_{ij}$  and the induced metric  ${}^3g_{ij}$  on the slice. Since this will require the application of Einstein's equations we will specialize to the case of vacuum gravity. In §4.1.1 we will describe the general method for determining the Teukolsky function from data on the initial slice then in §4.1.2 we will discuss a simplified form of this procedure applicable to linear perturbations of a Kerr spacetime.

### 4.1.1 Generic treatment

The key component of the Teukolsky function is  $\Psi_4$ , a particular projection of the Weyl in relation to a null tetrad basis,

$$\Psi_4 = {}^4C_{abcd} n^a \bar{m}^b n^c \bar{m}^d \quad (4.1)$$

where  ${}^4C_{abcd}$  is the Weyl tensor in the perturbed spacetime,  $n^a$  and  $\bar{m}^a$  are two of the principal null vectors as defined by Chandrasekhar[24] for instance, and  $f(r)$  is a specific function defined in the unperturbed Kerr spacetime. Since we are considering specifically the case of vacuum gravity the Weyl tensor is identical to the Riemann tensor  ${}^4R_{abcd}$ . Thus the primary work of calculating the Teukolsky function is to determine the 4-Riemann tensor from the 3-metric  ${}^3g_{ij}$ , the extrinsic curvature  $K_{ij}$ , and Einstein's equations on the initial slice. We will find a representation of  ${}^4R_{abcd}$  in terms of  ${}^3g_{ij}$ ,  $K_{ij}$ , and  $\hat{n}^a$  the normal to the initial hypersurface. By repeated application of the relation  $\delta_a^b = {}^3\delta_a^b - n_a n^b$  giving projections of the Riemann tensor into pieces normal or tangent to the initial hypersurface, we can decompose  ${}^4R_{abcd}$  into three pieces

$$\begin{aligned} \perp {}^4R_{ijkl} &:= {}^4R_{abcd} h_i^a h_j^b h_k^c h_l^d \\ \perp {}^4R_{ijk\hat{n}} &:= {}^4R_{abcd} h_i^a h_j^b h_k^c \hat{n}^d \end{aligned} \quad (4.2)$$

$$\perp {}^4R_{ij\hat{n}\hat{n}} := {}^4R_{abcd} h_i^a h_j^b \hat{n}^c \hat{n}^d \quad (4.3)$$

These quantities are sufficient to specify the Riemann tensor since all other components on  ${}^4R_{abcd}$  can be determined from them by applying the Riemann symmetries. Reexpressing  $\Psi_4$  function in terms of these projections we have

$$\begin{aligned}\Psi_4 &= \perp {}^4R_{ijkl} n^i \bar{m}^j n^k \bar{m}^l \\ &+ \perp {}^4R_{i\hat{n}j\hat{n}} \left[ (n^{\hat{n}})^2 \bar{m}^i \bar{m}^j + (\bar{m}^{\hat{n}})^2 n^i n^j - n^{\hat{n}} \bar{m}^{\hat{n}} (n^i \bar{m}^j + n^j \bar{m}^i) \right] \\ &+ 2 \perp {}^4R_{ijk\hat{n}} n^j \bar{m}^i (n^{\hat{n}} \bar{m}^k - \bar{m}^{\hat{n}} n^k)\end{aligned}$$

where  $n^{\hat{n}} = n^a \hat{n}_a$  and  $\bar{m}^{\hat{n}} = m^a \hat{n}_a$ . The Gauss and Codazzi relations allow us to express  $\perp {}^4R_{ijkl}$  and  $\perp {}^4R_{ijk\hat{n}}$ , respectively, in terms of the spatial quantities.

$$\begin{aligned}\perp {}^4R_{ijkl} &= {}^3R_{ijkl} + K_{ik}K_{jl} - K_{il}K_{jk} \\ \perp {}^4R_{ijk\hat{n}} &= D_j K_{ik} - D_i K_{jk}\end{aligned}\tag{4.4}$$

where  $D_i$  is the derivative operator on the spatial slice consistent with  ${}^3g_{ij}$ . To relate  $\perp {}^4R_{i\hat{n}j\hat{n}}$  to spatial quantities requires Einstein's equations. Using  ${}^4g_{ab} + \hat{n}_a \hat{n}_b = {}^3g_{ab}$ , we have

$$\begin{aligned}\perp {}^4R_{i\hat{n}j\hat{n}} &= \perp {}^4R_{iajb} ({}^3g^{ab} - {}^4g^{ab}) \\ &= \perp {}^4R_{iajb} {}^3g^{ab} - \perp {}^4R_{ij} \\ &= \perp {}^4R_{ikjl} {}^3g^{kl}.\end{aligned}\tag{4.5}$$

This completes the determination of  $\Psi_4$  in terms of  ${}^3g_{ij}$  and  $K_{ij}$ .

### 4.1.2 Perturbations

What we are really interested in though is the Teukolsky function for linear perturbations of the Kerr spacetime. For the Kerr spacetime, all components of the Weyl tensor vanish except one which is given by

$$\Psi_2 = {}^4R_{abcd} l^a m^b n^c \bar{m}^d. \quad (4.6)$$

This component is special in the sense that it requires contraction with all four distinct principal null vectors. For the background Kerr spacetime then all components of Weyl tensor in the tetrad basis with a repeated principal null vector index will vanish, as is the case for  $\Psi_4$ . Now, looking at perturbations of  $\Psi_4$  we see

$$\delta\Psi_4 = (\delta^4R_{abcd}) n_{(0)}^a \bar{m}_{(0)}^b n_{(0)}^c n_{(0)}^d + {}^4R_{(0)abcd} \delta(n^a \bar{m}^b n^c \bar{m}^d) \quad (4.7)$$

$$= (\delta^4R_{abcd}) n_{(0)}^a \bar{m}_{(0)}^b n_{(0)}^c \bar{m}_{(0)}^d. \quad (4.8)$$

The second term vanishes for linear perturbations because regardless of how  $\delta n^a$  and  $\delta \bar{m}^a$  decompose into tetrad components there will always be a duplicated basis vector in the set of four which are contracted with the Riemann tensor and thus none on the only non-vanishing Weyl component  $\Psi_2$ .

For the rest of the calculation we will assume some choice of time coordinate, though we will later show that first order perturbations of our time choice do not affect the result. The time coordinate is specified by  $t^a = \alpha \hat{n}^a + \beta^a$  which we will take as a

first order perturbation of the Boyer-Lindquist time coordinate for the Kerr spacetime.

Then, in components,  $\Psi_4$  is,

$$\begin{aligned}
\Psi_4 = & \quad {}^4R_{ijkl} n^i \bar{m}^j n^k \bar{m}^l \\
& + 2 {}^4R_{0ijk} n^j \bar{m}^k (n^0 \bar{m}^i - \bar{m}^0 n^i) \\
& + {}^4R_{i0j0} \left[ (n^0)^2 \bar{m}^i \bar{m}^j + (\bar{m}^0)^2 n^i n^j - n^0 \bar{m}^0 (n^i \bar{m}^j + n^j \bar{m}^i) \right] \quad (4.9)
\end{aligned}$$

where the  $ijk$  indices run over the spatial coordinates. Applying the explicit representation of the time coordinate in terms of lapse and shift gives the Riemann components

$$\begin{aligned}
{}^4R_{0ijk} &= \alpha \perp {}^4R_{\hat{n}ijk} + \beta^l \perp {}^4R_{likj} \quad \text{and} \quad (4.10) \\
{}^4R_{i0j0} &= \alpha^2 \perp {}^4R_{i\hat{n}j\hat{n}} + \alpha \beta^k (\perp {}^4R_{\hat{n}ikj} + \perp {}^4R_{\hat{n}jki}) + \beta^k \beta^l \perp {}^4R_{ikjl}.
\end{aligned}$$

Putting together Eq. 4.4 and Eq. 4.5 with Eq. 4.9 and Eq. 4.10 results in the following expression.

$$\begin{aligned}
\Psi_4 = & \quad A_{ijkl} n^i \bar{m}^j n^k \bar{m}^l + 2B_{ijk} n^j \bar{m}^k (n^0 \bar{m}^i - n^i \bar{m}^0) \\
& + C_{ij} ((n^0)^2 \bar{m}^i \bar{m}^j + (\bar{m}^0)^2 n^i n^j - n^0 \bar{m}^0 (n^i \bar{m}^j + n^j \bar{m}^i)) \quad (4.11)
\end{aligned}$$

where

$$A_{ijkl} = {}^3R_{ijkl} + [K_{jl} K_{ik} - K_{il} K_{jk}]$$

$$\begin{aligned}
B_{ijk} &= \alpha[D_j K_{ik} - D_k K_{ij}] + \beta^l A_{lijk} \\
C_{ij} &= \alpha^2 A_{iljm} {}^3g^{lm} - B_{ijl} \beta^l - B_{jil} \beta^l - A_{iljm} \beta^l \beta^m
\end{aligned}$$

Using Eq. 4.11, we obtain the following expression of the first order perturbation of  $\Psi_4$  in terms of perturbations in the 3-metric  $\delta g_{ij}$ , perturbations in the extrinsic curvature  $\delta K_{ij}$ , and several quantities from the the background (Kerr) geometry, the spatial metric  ${}^3g_{(0)ij}$ , the extrinsic curvature  $K_{(0)ij}$ , the lapse  $N_{(0)}$  and the shift  $N_{(0)i}$ . We have already argued that first order perturbations of the principal null vectors  $n^a$  and  $\bar{m}^a$  will not contribute to  $\delta\Psi_4$  so we have

$$\begin{aligned}
\delta\Psi_4 &= \delta A_{ijkl} n^i \bar{m}^j n^k \bar{m}^l + 2\delta B_{ijk} n^j \bar{m}^k [n^0 \bar{m}^i - n^i \bar{m}^0] \\
&\quad + \delta C_{ij} [n^0 \bar{m}^i n^0 \bar{m}^j + n^i \bar{m}^0 n^j \bar{m}^0 - n^0 \bar{m}^i n^j \bar{m}^0 - n^0 \bar{m}^j n^i \bar{m}^0] \quad (4.12)
\end{aligned}$$

where

$$\begin{aligned}
\delta A_{ijkl} &= \delta^3 R_{ijkl} + [K_{(0)jl} \delta K_{ik} + K_{(0)ik} \delta K_{jl} - (k \leftrightarrow l)] \\
\delta B_{ijk} &= \alpha_{(0)} [D_j \delta K_{ik} - \frac{1}{2} [D_k \delta^3 g_{mi} + D_i \delta^3 g_{mk} - D_m \delta^3 g_{ik}] {}^3g_{(0)}{}^{lm} K_{(0)lj} - (k \leftrightarrow j)] \\
&\quad + \beta_{(0)}{}^l \delta A_{lijk} + A_{(0)lijk} \delta^3 g^{lm} \beta_{(0)m} \\
\delta C_{ij} &= \alpha_{(0)}^2 A_{(0)iljm} \delta^3 g^{lm} + \alpha_{(0)}^2 \delta A_{iljm} {}^3g_{(0)}{}^{lm} \\
&\quad - [\delta B_{ijl} \beta_{(0)}{}^l + B_{(0)ijl} \delta^3 g^{lm} \alpha_{(0)m} + A_{(0)jil} \delta^3 g^{lm} \beta_{(0)m} + \delta A_{jil} \beta_{(0)}{}^l \\
&\quad + \delta A_{iljm} \beta_{(0)}{}^l \beta_{(0)}{}^m + A_{(0)iljm} \alpha_{(0)k} \delta^3 g^{kl} \beta_{(0)}{}^m + A_{(0)iljm} \alpha_{(0)}{}^l \delta^3 g^{km} \beta_{(0)k}]
\end{aligned}$$



and

$$\delta^3 R_{jkl}^i = \frac{1}{2} D_k [{}^3g_{(0)}^{im} (D_l \delta^3 g_{mj} + D_j \delta^3 g_{ml} - D_m \delta^3 g_{jl})] - (k \leftrightarrow l)$$

To calculate  $\dot{\Psi}_4$  we use the above expression for  $\delta\Psi_4$  and plug in  $\delta^3\dot{g}_{ij}$  and  $\delta\dot{K}_{ij}$  for  $\delta^3g_{ij}$  and  $\delta K_{ij}$  in the above, respectively. Obtaining  $\delta^3\dot{g}_{ij}$  and  $\delta\dot{K}_{ij}$  from Einstein's equations as follows:

$$\begin{aligned} \delta^3\dot{g}_{ij} &= -2\alpha_{(0)} \delta K_{ij} + \beta_{(0)}^k \delta^3 g_{ij,k} + \beta_{(0)l} \delta^3 g^{lk} {}^3g_{(0)ij,k} + \delta^3 g_{ik} \beta_{(0)}^k{}_{,j} \\ &\quad + {}^3g_{(0)il} [\delta^3 g^{kl} \beta_{(0)k}]_{,j} + {}^3g_{(0)lj} [\delta^3 g^{kl} \beta_{(0)k}]_{,i} + \delta^3 g_{kj} \beta_{(0)}^k{}_{,i} \\ \delta\dot{K}_{ij} &= \frac{1}{2} [D_j \delta^3 g_{mi} + D_i \delta^3 g_{mj} - D_m \delta^3 g_{ij}] {}^3g_{(0)}^{mk} \beta_{(0),k} \\ &\quad + \alpha_{(0)} [\delta^3 R_{ij} - 2K_{(0)}^k{}_j \delta K_{ik} - 2\delta K^k{}_j K_{(0)ik} + K_{(0)ij} \delta K + K_{(0)} \delta K_{ij}] \\ &\quad + \beta_{(0)}^k \delta K_{ij,k} + \delta K_{ik} \beta_{(0)}^k{}_{,j} + \delta K_{kj} \beta_{(0)}^k{}_{,i} + K_{(0)il} [\delta^3 g^{kl} \beta_{(0)k}]_{,j} \\ &\quad + K_{(0)lj} [\delta^3 g^{kl} \beta_{(0)k}]_{,i} + \beta_{(0)l} \delta^3 g^{lk} K_{(0)ij,k} \end{aligned}$$

where  $\delta K = {}^3g_{(0)}^{ij} \delta K_{ij} + K_{(0)ij} \delta^3 g^{ij}$  and  $\delta K^i{}_j = \delta K_{jk} {}^3g_{(0)}^{ki} + K_{(0)jk} \delta^3 g^{ki}$ .

### 4.1.3 Discussion

The key property which allows us to write  $\Psi_4$  and hence the Teukolsky function purely in terms of the data on a Cauchy slice is that  $\Psi_4$  is invariant under first order transformations of the background tetrad. An analogous treatment is applicable to  $\Psi_0$  which has the same property. The vanishing of all background Weyl components other than  $\Psi_2$  also guarantees the first order gauge invariance of  $\dot{\Psi}_4$ . Gaurav Khanna has

explicitly verified by computer algebra the independence of the result for  $\Psi_4$  and  $\dot{\Psi}_4$  obtained as described here.[28]

## 4.2 A New Approach to Kerr-Limit Data

<sup>1</sup> For problems of astrophysical interest it is paramount to begin with initial data which correspond to a realistic astrophysical configuration. If the black holes begin very far apart we could approximate each as a stationary spherically symmetric black hole and there would be no ambiguity in the initial data. But once the black holes are close enough to interact significantly it is difficult to say what are astrophysically realistic initial data. Most of the numerical calculations for binary black hole collisions that have been attempted thus far have begun evolving from initial data constructed via the conformal flatness formalism. A special case of this, the so called Bowen-York method <sup>3</sup> specifies how to derive a family of solutions to the initial value equations which have a conformally flat spatial metric and vanishing mean curvature and which can be interpreted as boosted or spinning black holes. There are problems with the assumption of conformal flatness though, particularly for spinning black holes. For an initial data set to be astrophysically realistic, a minimum requirement is that sufficiently separated black holes look like Kerr black holes. Since we do not know of a foliation of the Kerr spacetime which admits conformally flat spacelike slices, we are unable to exactly represent Kerr black holes in such a formalism. This difference between Kerr black holes and Bowen-York spinning black holes is demonstrated by the nonzero gravitational radiation emitted by a single black hole.<sup>4</sup>

In this section we describe a novel method for solving the initial value equations of general relativity for a broad class of 3-metrics which includes axisymmetric slices.

---

<sup>1</sup>The material in this section is reproduced with permission and some reworking from Ref. [29]. Copyright ©1999 by the American Physical Society.

Unlike the Bowen-York approach, where the extrinsic curvature is selected first and then the metric is calculated from the constraints, we first choose the metric and then calculate the extrinsic curvature. After introducing our technique, we apply it to the Kerr black hole demonstrating that the Kerr hole does indeed come out as a special case. By comparison with this solution, we propose a method which may be used to introduce multiple Kerr-like black holes on the initial hypersurface. In particular, if the black holes are sufficiently separated, then in the neighborhood of each one, we ask that the data approach those for a Kerr hole. Moreover, if the two holes are sufficiently close, the data should also resemble that for a single black hole.

#### 4.2.1 Solving the Constraints

<sup>2</sup> Here we shall find a general solution to the constraint equations for a Cauchy slice whose intrinsic geometry admits a surface-orthogonal Killing field. In particular, this is true of the surfaces of constant Boyer-Lindquist time in the Kerr spacetime. Later, we will construct initial data with spatial geometry satisfying this same condition for two black holes.

For definiteness we will assume that our Killing vector field corresponds to an axial symmetry, though this restriction on the topology of the is not essential to our construction. Let  $\phi$  be the azimuthal coordinate so that  $\partial/\partial\phi$  is the Killing field. The existence of orthogonal surfaces implies that our spatial metric can be cast in the form  $q_{ij}dx^i dx^j = \tilde{h}_{ij}dx^i dx^j + B d\phi^2$ , where the two-metric  $\tilde{h}_{ij}$  is restricted to surfaces of

---

<sup>2</sup>The material in this subsection was developed in intensive collaboration with Ray Puzio, and is presented here as necessary background material for the rest of this section.

constant  $\phi$ . Since these surfaces have the topology of half-planes, we can write  $\tilde{h}_{ij} = Ah_{ij}$  where  $h_{ij}$  is a flat metric and  $A$  is a suitable conformal factor. If we choose two of the three spatial coordinates to be constant along the orbits of the isometry, then the components of  $h_{ij}$  in our coordinate system as well as the functions  $A$  and  $B$  will not depend on  $\phi$ . If we choose rectangular coordinates in the half-plane, then our metric assumes the form

$$q_{ij} dx^i dx^j = A(x, y)(dx^2 + dy^2) + B(x, y)d\phi^2 \quad . \quad (4.13)$$

The initial value equations of geometrodynamics are a set of four coupled partial differential equations which relate the metric  $q_{ij}$  and extrinsic curvature  $K_{ij}$  of a hypersurface embedded in a vacuum spacetime. In tensor notation they are written as a vector equation known as the momentum constraint and a scalar equation known as the Hamiltonian constraint:

$$\begin{aligned} \nabla^j K_{ij} &= \partial_i (q^{jk} K_{jk}) \\ (q^{ac} q^{bd} - q^{ab} q^{cd}) K_{ab} K_{cd} &= {}^{(3)}\mathcal{R}[q] \end{aligned}$$

From here we will proceed as follows. First we will show that the momentum constraint reduces to a set of Cauchy-Riemann equations to be solved for  $K_{xx}$ ,  $K_{yy}$ , and  $K_{xy}$  and the condition that  $K_{x\phi}$  and  $K_{y\phi}$  can be derived from a potential. Then the Hamiltonian constraint provides a condition which determines this potential. In the

coordinate system introduced last paragraph, the momentum constraint looks as follows:

$$\left\{ \begin{array}{l} \frac{\partial(B^{\frac{1}{2}}K_{xx})}{\partial x} + \frac{\partial(B^{\frac{1}{2}}K_{xy})}{\partial y} = A \frac{\partial(B^{\frac{1}{2}}K)}{\partial x} - \frac{1}{2} \frac{\partial(\log(B/A))}{\partial x} B^{\frac{1}{2}}(K_{xx} + K_{yy}) \\ \frac{\partial(B^{\frac{1}{2}}K_{xy})}{\partial x} + \frac{\partial(B^{\frac{1}{2}}K_{yy})}{\partial y} = A \frac{\partial(B^{\frac{1}{2}}K)}{\partial y} - \frac{1}{2} \frac{\partial(\log(B/A))}{\partial y} B^{\frac{1}{2}}(K_{xx} + K_{yy}) \\ \frac{\partial(B^{\frac{1}{2}}K_{x\phi})}{\partial x} + \frac{\partial(B^{\frac{1}{2}}K_{y\phi})}{\partial y} = 0 \end{array} \right. \quad (4.14)$$

The general solution for the third equation can be written at once in terms of a potential function  $u(x, y)$ :

$$\left\{ \begin{array}{l} K_{x\phi} = +B^{-\frac{1}{2}} \frac{\partial u}{\partial y} \\ K_{y\phi} = -B^{-\frac{1}{2}} \frac{\partial u}{\partial x} \end{array} \right. \quad (4.15)$$

The other two equations involve the remaining four components of the extrinsic curvature. Since there are two more quantities than equations, we may take two of the quantities as known and solve for the remaining two. It proves advantageous to take the quantities  $P$  and  $Q$  defined as  $P := B^{\frac{1}{2}}(K_{xx} - K_{yy})/2$  and  $Q := B^{\frac{1}{2}}K_{xy}$  as our unknowns since our equations then take the following form:

$$\left\{ \begin{array}{l} \frac{\partial P}{\partial x} + \frac{\partial Q}{\partial y} = j(x, y) \\ \frac{\partial Q}{\partial x} - \frac{\partial P}{\partial y} = k(x, y) \end{array} \right. \quad (4.16)$$

where the sources  $j$  and  $k$  are defined as

$$\begin{aligned} j &:= A \frac{\partial(B^{\frac{1}{2}}K)}{\partial x} - \frac{1}{2} \frac{\partial(\log(B/A))}{\partial x} B^{\frac{1}{2}}(K_{xx} + K_{yy}) - \frac{1}{2} \frac{\partial(B^{\frac{1}{2}}K_{xx} + B^{\frac{1}{2}}K_{yy})}{\partial x} \\ k &:= A \frac{\partial(B^{\frac{1}{2}}K)}{\partial y} - \frac{1}{2} \frac{\partial(\log(B/A))}{\partial y} B^{\frac{1}{2}}(K_{xx} + K_{yy}) + \frac{1}{2} \frac{\partial(B^{\frac{1}{2}}K_{xx} + B^{\frac{1}{2}}K_{yy})}{\partial y} \end{aligned}$$

$$K := A(K_{xx} + K_{yy}) + BK_{\phi\phi} \quad (4.17)$$

These equations have the form of Cauchy-Riemann equations with source and can hence be solved by well-known methods of potential theory. For instance, we might write  $P$  and  $Q$  as integrals of  $j$  and  $k$  against Green's functions.

$$\begin{aligned} P(x, y) &= \oint_{\partial\mathbf{D}} ds \left\{ G_{\mathbf{R}}(x, y, x', y')n(x', y') - G_{\mathbf{I}}(x, y, x', y')m(x', y') \right\} \\ &\quad - \int_{\mathbf{D}} dx' dy' \left\{ G_{\mathbf{R}}(x, y, x', y')k(x', y') - G_{\mathbf{I}}(x, y, x', y')j(x', y') \right\} \\ Q(x, y) &= \oint_{\partial\mathbf{D}} ds \left\{ G_{\mathbf{R}}(x, y, x', y')m(x', y') + G_{\mathbf{I}}(x, y, x', y')n(x', y') \right\} \\ &\quad - \int_{\mathbf{D}} dx' dy' \left\{ G_{\mathbf{R}}(x, y, x', y')j(x', y') - G_{\mathbf{I}}(x, y, x', y')k(x', y') \right\} \\ K_{xy} &= B^{-\frac{1}{2}}Q \quad (4.18) \\ K_{xx} &= \frac{K - BK_{\phi\phi}}{2A} + B^{-\frac{1}{2}}P \\ K_{yy} &= \frac{K - BK_{\phi\phi}}{2A} - B^{-\frac{1}{2}}P \end{aligned}$$

The choice of Green function will depend on the domain  $\mathbf{D}$  over which  $x$  and  $y$  range and the conditions imposed on its boundary. In addition to this solution of the inhomogeneous equations, we might also require a solution of the homogeneous system. For applications related to the two-body problem, it is natural to consider the half-plane  $y > 0$  as our domain and ask that the extrinsic curvature go to zero as  $y \rightarrow \infty$ . With these specifications, the relevant choice of Green function is given as

$$G_{\mathbf{R}}(x, y, x', y') = \frac{y'[(x-x')^2 + y^2 - x^2]}{\pi[(x-x')^2 + (y-y')^2][(x-x')^2 + (y+y')^2]}$$

$$G_{\mathbf{I}}(x, y, x', y') = \frac{2yy'(x-x')}{\pi[(x-x')^2+(y-y')^2][(x-x')^2+(y+y')^2]}$$

Before proceeding further with our calculations, let us pause to consider our ultimate goal. We began by specifying a metric by a choice of  $A$  and  $B$ . Next, we chose  $K$  and  $K_{xx} + K_{yy}$ . The solution of the equations above for  $P$  and  $Q$  determine two more components of the extrinsic curvature. The only thing we still need for a complete specification of the initial data is the  $u$  potential. We shall now proceed to determine  $u$  by solving the remaining initial value equation, which is the Hamiltonian constraint.

The Hamiltonian constraint can be regarded as an equation for the hitherto arbitrary function  $u(x, y)$ . Substituting Eq. 4.15 into the Hamiltonian constraint and rearranging, we arrive at the formula

$$\left(\frac{\partial u}{\partial x}\right)^2 + \left(\frac{\partial u}{\partial y}\right)^2 = 2v(x, y) \quad (4.19)$$

$$\begin{aligned} 2v(x, y) &:= AB^2 {}^{(3)}\mathcal{R} - \frac{2B^2}{A} \left[ (K_{xx})^2 + K_{xx}K_{yy} + (K_{yy})^2 + (K_{xy})^2 \right] \\ {}^{(3)}\mathcal{R} &= -\frac{1}{2AB^{\frac{1}{2}}} \left\{ \frac{\partial^2 B^{\frac{1}{2}}}{\partial x^2} + \frac{\partial^2 B^{\frac{1}{2}}}{\partial y^2} \right\} - \frac{1}{4A} \left\{ \frac{\partial^2(\log A)}{\partial x^2} + \frac{\partial^2(\log A)}{\partial y^2} \right\} \end{aligned}$$

Eq. 4.19 has the form of a Hamilton-Jacobi equation for a particle moving in a two-dimensional potential. As is well known from analytical dynamics, such a partial differential equation can be solved using the method of characteristics. Given a solution  $u(x, y)$  to the equation, the characteristics are a congruence of curves with the property that the tangent vector at any point on one of these curves equals the gradient of  $u(x, y)$ .



If we label the various curves in the congruence by a parameter  $s$  and describe them by the equations

$$\begin{cases} x = X(t; s) \\ y = Y(t; s) \end{cases} \quad (4.20)$$

then this property is expressed analytically as

$$\begin{aligned} \frac{\partial u}{\partial x} &= \frac{dX}{dt} \\ \frac{\partial u}{\partial y} &= \frac{dY}{dt} \end{aligned}$$

From these equations above and the non-linear partial differential Eq. 4.19, it follows that

$$\begin{aligned} \frac{d^2 X}{dt^2} &= \frac{\partial v}{\partial x} \\ \frac{d^2 Y}{dt^2} &= \frac{\partial v}{\partial y} \end{aligned}$$

To solve the partial differential equation, we can reverse the logic of the last paragraph. Start with a one parameter family of solutions to the second order ordinary differential equation, Eq. 4.21. (These solutions can be thought of as the trajectories of a fluid of particles moving in a potential well  $-v(x, y)$ .) Differentiating with respect to  $t$ , obtain a vector field  $(dX/dt, dY/dt)$ . This vector field will have vanishing curl and, by integrating, one can obtain the scalar  $u(x, y)$  of which it is the gradient. For our purposes, however, only the gradient of  $u$  and not  $u$  itself is required, so there is

no reason to actually carry out the integration. Recalling Eq. 4.15, we can write the following formula for two components of the extrinsic curvature tensor:

$$\begin{aligned} K_{x\phi} &= +B^{-\frac{1}{2}} \frac{dY}{dt} \\ K_{y\phi} &= -B^{-\frac{1}{2}} \frac{dX}{dt} \end{aligned}$$

Along with Eq. 4.17 and Eq. 4.18, the above formula can be used to compute the extrinsic curvature given the four freely specifiable functions  $A(x, y)$ ,  $B(x, y)$ ,  $K(x, y)$ , and  $K_{\phi\phi}(x, y)$  and having obtained a one-parameter family of solutions to the system in Eq. 4.21.

#### 4.2.2 The Single Black Hole

In the last section, we described a method for solving for the extrinsic curvature that involved a Hamilton-Jacobi equation and mentioned that the method is applicable to Kerr spacetimes. In this section, we will consider the geometry of a hypersurface in this spacetime from the standpoint of our method. In the next section, we will utilize this representation of the initial value problem for a Kerr spacetime to construct initial data for the two black hole problem.

A stationary and axisymmetric spacetime admits a preferred foliation in which time is given by locally non-rotating vector field. For the case of Kerr, this is known as Boyer-Lindquist time. In terms of our formalism the intrinsic geometry on such a

constant time slice of Kerr can be written as

$$\begin{aligned}
q_{ij} dx^i dx^j &= Ah_{ij} dx^i dx^j + B d\phi^2 \\
A &= \frac{r^2 + a^2 \cos^2 \theta}{R^2} \\
B &= \left( \frac{r^2 + a^2}{R^2} + \frac{2mra^2 \sin^2 \theta}{AR^4} \right) AR^2 \sin^2 \theta \\
h_{ij} dx^i dx^j &= dR^2 + R^2 d\theta^2 \\
R &:= \frac{1}{4} \left( \sqrt{r - 2m + 2\sqrt{m^2 - a^2}} + \sqrt{r - 2m - 2\sqrt{m^2 - a^2}} \right)^2
\end{aligned} \tag{4.21}$$

where  $r$  is the usual Boyer-Lindquist radial function and  $R, \theta$  are polar coordinates in the half-planes of constant  $\phi$ . The metric  $h_{ij}$  in these planes is seen to be manifestly flat.

Since we will be considering multiple black holes, it may be helpful to discuss this form for the spatial part of the Kerr metric a little further. If  $A \equiv B$ , the spatial metric would be conformally flat. That  $A$  and  $B$  differ makes the conformal flatness formalism inapplicable. It is interesting to note the limiting behavior of these functions.

$$\begin{aligned}
A &= 1 + \frac{2m}{r} + \mathcal{O}\left(\frac{1}{r^2}\right) && r \rightarrow \infty \\
B &\geq AR^2 \sin^2 \theta && \text{everywhere} \\
\frac{B}{AR^2 \sin^2 \theta} &= 1 + \frac{a^2 \sin^2 \theta}{r^2} + \mathcal{O}\left(\frac{1}{r^3}\right) && r \rightarrow \infty \\
\frac{B}{AR^2 \sin^2 \theta} &\rightarrow 1 + \mathcal{O}(a^2) && a \rightarrow 0 \\
\frac{B}{AR^2 \sin^2 \theta} &\rightarrow 1 + \mathcal{O}(\sin^2 \theta) && \theta \rightarrow 0
\end{aligned}$$

Thus we see that  $B \neq AR^2 \sin^2 \theta$ , but differs from  $AR^2 \sin^2 \theta$  minimally except in a region near each hole and off the symmetry axis. Note that this description of the Kerr data is similar to that studied by Brandt and Seidel<sup>6</sup>. They studied initial data where

the Kerr spatial metric was modified by the addition of a Brill wave, which changes the ratio  $B/A$ .

In Boyer-Lindquist coordinates, the only non-vanishing components of the extrinsic curvature for a hypersurface of constant  $t$  are  $K_{r\phi}$  and  $K_{\theta\phi}$ . From Eq. 4.15 of last section, we know that these can be expressed in terms of a potential function  $u(r, \theta)$ . Doing the computation, we find that the potential responsible for these two non-vanishing components is

$$u(r, \theta) = \frac{(1 + \cos \theta)^2}{r^2 + a^2 \cos^2 \theta} (r^2 \cos \theta - a^2 \cos \theta - 2r^2) \quad .$$

We know that this potential function is the solution to a Hamilton-Jacobi equation. To find out which solution, we can inquire into the congruence of characteristic curves with which it is associated. Recall that these curves are orthogonal to the level curves of  $u$ . Having the explicit expressions at hand, we could formulate this orthogonal trajectory problem concretely and attempt to solve it. However, for our purposes such details are unnecessary, and we shall content ourselves with a qualitative discussion.

First, let us note that in the region  $r > a$  and away from the axis of symmetry,  $u$  is non-singular and its gradient does not vanish. As a consequence, the curves we are interested in will be smooth and free from bifurcations and fixed points. To determine their topology, we shall consider the rays  $\theta = 0, \pi/2, \pi$ . On the ray  $\theta = \pi/2$ ,  $u$  is constant, so the characteristic curves must be orthogonal to this ray. Examining the metric  $h$ , we see this means that they must point along the  $\theta$  direction. Near the symmetry axis,

$\theta = 0$ , the gradient of  $u$  goes to zero, so we shall make an expansion in powers of  $\theta$ .

$$u(r, \theta) = -4 + \frac{3r^2 - a^2}{4r^2 + 4a^2}\theta^4 + \mathcal{O}(\theta^6)$$

From this, we see that the gradient of  $u$  is parallel to the symmetry axis for small  $\theta$  and that its norm vanishes like  $\theta^3$ . Hence the orthogonal trajectories will point at right angles towards or away from this axis. By symmetry, the same situation will occur near the other half of the axis,  $\theta = \pi$ . Combining these observations, we conclude that the various curves of our congruence start out perpendicular to one end of the symmetry axis, arch around the black hole, and return perpendicular to the other end of the symmetry axis.

To generate this initial data set for Kerr metric within our formalism, we first have to specify the spatial metric by choosing  $A$  and  $B$  as given in Eq. 4.21. Then, making the choices  $K = K_{\phi\phi} = 0$  and specifying that the congruence of curves needed for the construction of  $K_{r\phi}$  and  $K_{\theta\phi}$  meet the symmetry axis perpendicularly will guarantee that the correct extrinsic curvature comes out of the construction. The one remaining choice is the overall sign of the extrinsic curvature, which determines the sign of the angular momentum. This choice can be made by specifying on which side of the symmetry axis the characteristics originate.

### 4.2.3 Two Black Holes

Given an axially symmetric spatial metric, our formalism shows how to find an extrinsic curvature which will satisfy the initial value problem of general relativity. Our strategy for representing two rotating black holes will be to choose a spatial metric

which resembles the spatial metric of the Kerr solution in three regions. These are the two regions near the chosen locations for the black holes on the symmetry axis and the region near spatial infinity. Then we will use the methods described above to calculate an extrinsic curvature which satisfies the initial value problem. In general, there should be many solutions from which we will select one that is consistent with the description of the Kerr extrinsic curvature whenever the spatial metric approaches that of the Kerr solution.

The first step is to construct a three-metric which has the appropriate behavior in the near and far limits. One way to do this is to use the form given above for  $A$  and  $B$  of the Kerr metric and replace  $\frac{R}{m}$ ,  $\frac{a}{m}$ , and  $\sin \theta$ , with functions which approach the correct values in the limits near one of the holes or away from both. Let the Kerr metrics approached near each of the two holes have parameters  $(m_1, a_1)$  and  $(m_2, a_2)$ . Then we want the parameters of the metric approached at infinity to correspond to an appropriate sum of the masses and angular moments associated with the two holes. Thus we want

$$m_{\text{far}} = m_1 + m_2$$

and

$$a_{\text{far}} m_{\text{far}} = a_1 m_1 + a_2 m_2 \quad .$$

More explicitly then, if we rewrite the quantities  $A$  and  $B$  for the Kerr metric with  $m_{\text{far}}$  scaled to unity and replace  $R$ ,  $a$ , and  $\sin \theta$  with  $\tilde{R}$ ,  $\tilde{a}$ , and  $\tilde{s}$ , which are functions of

$x$  and  $y$ , we have

$$\begin{aligned}
 A &= \frac{\tilde{r}^2 + \tilde{a}^2(1 - \tilde{s}^2)}{\tilde{R}^2} \\
 B &= \left( \frac{\tilde{r}^2 + \tilde{a}^2}{\tilde{R}^2} + \frac{2\tilde{r}\tilde{a}^2\tilde{s}^2}{A\tilde{R}^4} \right) \rho^2 \\
 \tilde{r} &= \tilde{R} \left( 1 + \frac{1 + \tilde{a}}{\tilde{R}} \right) \left( 1 + \frac{1 - \tilde{a}}{\tilde{R}} \right)
 \end{aligned} \tag{4.22}$$

For convenience we have introduced the coordinate  $\rho = R \sin \theta$  which is the distance from the symmetry axis in the flat half-plane. In order for our initial data to behave properly in the three limits, we specify the following limits on the new functions:

$$\left. \begin{aligned}
 \tilde{R} &\rightarrow \frac{R_1}{m_1} \\
 \tilde{s}^2 &\rightarrow \frac{\rho^2}{R_1^2} \\
 \tilde{a} &\rightarrow \frac{a_1}{m_1}
 \end{aligned} \right\} \frac{R_1}{m_1} \rightarrow 0$$
  

$$\left. \begin{aligned}
 \tilde{R} &\rightarrow \frac{R_2}{m_2} \\
 \tilde{s}^2 &\rightarrow \frac{\rho^2}{R_2^2} \\
 \tilde{a} &\rightarrow \frac{a_2}{m_2}
 \end{aligned} \right\} \frac{R_2}{m_2} \rightarrow 0$$

$$\left. \begin{aligned} \tilde{R} &\rightarrow R \\ \tilde{s}^2 &\rightarrow \frac{\rho^2}{R^2} \\ \tilde{a} &\rightarrow a_1 m_1 + a_2 m_2 \end{aligned} \right\} \frac{R_1}{m_1} \text{ and } \frac{R_2}{m_2} \rightarrow \infty$$

In Cartesian coordinates  $\rho$  and  $z$  on the half-plane  $R_1$  and  $R_2$  are the distances from the chosen locations,  $z_1$  and  $z_2$ , of the black holes on the symmetry axis.

$$R_i = \sqrt{\rho^2 + (z - z_i)^2}$$

These conditions guarantee that the metric approaches an appropriate Kerr metric in each of the three limits.

A natural choice for the function  $\tilde{R}(R_1, R_2)$  with suitable limiting behavior is

$$\tilde{R} = \frac{1}{\frac{m_1}{R_1} + \frac{m_2}{R_2}} .$$

It can be seen from Eq. 4.21 that in the case of non-spinning black holes, where we expect  $\tilde{a}$  to vanish identically,  $B$  becomes equal to  $A$  and  $A$  reduces to the conformal factor associated with the familiar Brill-Lindquist initial data for non-spinning black holes.

We can satisfy the conditions for  $\tilde{s}^2$  and  $\tilde{a}$  by choosing

$$\tilde{s}^2 = \frac{\rho^2}{\tilde{R}^2} \quad \text{and}$$



$$\tilde{a} = \tilde{R} \left( \frac{a_1 m_1}{R_1} + \frac{a_2 m_2}{R_2^2} \right). \quad (4.23)$$

These choices for  $\tilde{R}$ ,  $\tilde{s}$ , and  $\tilde{a}$  specify a metric which meets our requirements and we will take this to be our spatial metric for the rest of the discussion. There are certainly other equally well-qualified and well-motivated choices of spatial geometry satisfying the conditions we have given.

Having specified a three-metric, we now want to find an extrinsic curvature which solves the constraints and resembles the extrinsic curvature for the Kerr case in the appropriate limits. Since  $K_{\phi\phi}$  and the mean curvature  $K$  vanish in the Kerr case, we again choose them to vanish here. This means we use the trivial solution to the Eq. 4.17 and Eq. 4.18. Then what remains is to find a solution of Eq. 4.19 which reduces to the  $K_{ij}$  for Kerr in the limits, choosing initial values designed to be consistent with the Kerr extrinsic curvature. Our efforts to numerically implement such a solution have revealed important concerns which were not sufficiently appreciated this method was being designed.

#### 4.2.4 Discontinuities

In §4.2.1 we interpreted Eq. 4.19 as the Hamilton-Jacobi equation governing the motion of particles in a potential and described a general method for solving the differential equation which is guaranteed to work in some neighborhood of the initial value curve in the half plane. The method is, however, not guaranteed to produce a continuous solution “in the large”, over the entire  $x - y$  half-plane in our case. The newly appreciated difficulties are most evident if we now recognize this differential equation by

its common name the “eikonal equation”, which governs the propagation of wavefronts in the geometric approximation to optics, and has countless other practical applications. Appropriate initial value information is simply the initial position of the wavefront. Intuition about the propagation of wavefronts makes our difficulty evident. The typical behavior of wavefronts is to cross over themselves. In our context caustics in the wavefronts mean discontinuities in the first derivatives of  $u$ , and hence in the components of  $K_{ij}$ , across the cut where the wavefronts self-intersect. For example, in the simplest case that the right hand side of Eq. 4.19, which gives the squared speed of the waves, is a constant and the initial wavefront is a closed curve, nontrivial discontinuities outside the central point will be obtained unless the initial wavefront is exactly circular. The typical cases have the wave speed varying only by some moderate percentage away from some otherwise constant value. Our case is unusual because this wave-speed tends toward zero away from the holes and at the axis. Because of this it is not immediately obvious whether the typical eikonal behavior of wavefronts is what we can expect here. Nevertheless there is good reason for concern about the practicality of finding solutions with the method proposed here.

The viability of our method hinges on the question of whether any discontinuities which might appear in solving Eq. 4.19 can be avoided or at least hidden behind horizons of the holes. Unfortunately there appears to be little in the way of analytic results about the complicated relationship between the initial wavefront, the wave-speed function and the location of discontinuities, which would allow us to give general guarantees of discontinuity avoidance. Reasonably, though, one expects that if the wave-speed term is a

sufficiently small perturbation of that for the single Kerr black hole, the expected discontinuities can be forced to appear arbitrarily far inside the hole’s apparent horizon. Still, it would be difficult to interpret such data as corresponding to two black holes without some stronger claim about the extrinsic curvature’s relationship to the two holes. It seems that it will only be possible to determine the severity of the discontinuity problem by numerical testing.

Fortunately, the practicality of some of the eikonal equation’s other applications has ensured that there are efficient standard techniques for finding numerical solutions.

#### 4.2.5 Discussion

It should be noted that while the general “first (fundamental) form first” method of solving the initial value problem described in §4.2.1 can lead to discontinuous solutions, all continuous solutions are also obtainable. As was done with the Kerr solution, any known axisymmetric solution of the initial value problem can be rederived according to this method.

It is fair to say that this proposed method for calculating axisymmetric multiple black hole initial data has some unattractive features. While the method of choosing the metric function described in §4.2.3 is straightforward, and produces the desired limiting behavior the particular choice of the substitution functions,  $\tilde{R}$  and  $\tilde{a}$ , is not strongly motivated, and certainly not unique. And, of course, the discontinuity problem is a serious concern. Nevertheless, the need for Kerr perturbation binary black hole data is compelling. The closest competing prescription recently proposed by Krivan and Price[27] also has unattractive features, particularly an undesired singularity in

the metric. In the case that we can manage to find solutions for “u” numerically, the discontinuity problem may perhaps be regarded as comparable to the problems with the Krivan-Price data. If it turns out that the discontinuity problem can be avoided in practice, it may also be possible to extend the technique to non-axisymmetric data. Relaxing the assumption of axisymmetry in §4.2.1 leads to new couplings among the initial value equations, but the problem is under investigation.

## Chapter 5

### Future Directions

In Chapter 2 we have succeeded extending the work of Price and Pullin[6], using Schwarzschild perturbation theory to study collisions of black holes with some initial linear or angular momentum. The results not only verified the results of numerical integrations of Einstein's equations, but made it possible to explain several otherwise unexpected features of the numerical results. The linear analysis helped to put some physics back into the stream of numbers coming out of the supercomputer. With improving numerical techniques it becomes possible to study ever more interesting types of black hole collisions. It is expected that the type of comparisons made in Chapter 2, perhaps including also higher order perturbation studies, will continue to have an important role in explaining the outcome of numerical calculations. The considerable angular momentum which can be expected in remnants of inspiraling collisions makes Kerr perturbation studies essential if we wish to provide numerical inspiral studies with the same kind of benchmarking and interpretive support as Schwarzschild perturbations provide for collisions which result to static black hole remnants. The expectation of black hole remnants with significant angular momentum provides the need for new initial data sets which have a Kerr close limit. A proposal for axisymmetric black hole data with a Kerr close limit has been discussed in Chapter 4. We continue to work on numerically implementing this method to determine the significance of potential discontinuities. In

any case continuing efforts are needed to find families of “inspiraling” black hole data sets which can be approached by Kerr perturbation analysis in the close limit.

## Appendix

### Inversion Symmetry of $\hat{K}_{ij}$

Typically the inversion symmetry is imposed on the conformal extrinsic curvature as well as the conformal factor. This is achieved by adding to  $\hat{K}_{ij}$  a series of terms corresponding to the images of  $\hat{K}_{ij}$  generated by repeated reflections through the throats. In practice, to show that there is nothing to add all we have to do is to recognize that the image terms will be of higher order in  $\frac{L}{M}$ . To see this we need to look a little more closely at the imaging process. In the notation of Kulkarni's paper[30], which proves the convergence of the imaging process for  $\hat{K}_{ij}$ , the series of inversion-image terms of  $\hat{K}_{ij}$  is obtained by successive application of the operator  $\mathcal{R}_\alpha$  for performing a reflection through the  $\alpha^{\text{th}}$  throat. From Kulkarni's Eq. 12,

$$(\mathfrak{R}_\alpha \hat{K}_{ij})(\vec{x}) = \pm \left( \frac{a_\alpha}{r_\alpha} \right)^6 \mathcal{R}_x^\alpha \hat{K}_{ij}(J_\alpha \vec{x}) \mathcal{R}_x^\alpha \quad (\text{A.1})$$

Here  $a$  is the radius of the throats,  $J_\alpha$  is the inversion map through the  $\alpha^{\text{th}}$  throat, and  $\mathcal{R}_x^\alpha$  performs the reorientation of the tensor in the new coordinates without affecting the scale. Since we are only interested here in how Eq. A.1 determines the relative size of the image terms, the details of  $\mathcal{R}_x^\alpha$  are not important. For inversion through the first throat

$$J_1^* : r_1 \rightarrow \frac{a_1}{r_1} \quad (\text{A.2})$$

$$J_1^* : r_2 \rightarrow \mathcal{O}\left(\frac{L}{M}\right). \quad (\text{A.3})$$

In the end we only want to evaluate our final expression for  $\hat{K}_{ij}$  at points far outside the throats, where  $r > m \gg L > a$ . In this case  $J_1$  is a map from far outside the throat to far inside the throat. To determine the relative size of the image terms we need to consider how the four terms in the unsymmetrized Bowen-York  $\hat{K}_{ij}$  rescale when they are pulled back by  $J_1^*$ . Looking at Eq. 2.7, Eq. 2.8, and Eq. 2.9 we see that the four terms arising from the linear and angular momenta of each hole scale as

$$\begin{aligned} K_{P1} &\sim \frac{M P_1}{r_1^2} \\ K_{J1} &\sim \frac{M J_1}{r_1^3} \\ K_{P2} &\sim \frac{M P_2}{r_2^2} \\ K_{J2} &\sim \frac{M J_2}{r_2^3} \end{aligned} \quad (\text{A.4})$$

where we have given the four contributions to the conformal extrinsic curvature obvious names. Applying  $J_1^*$  to these and bringing in the additional factor of  $a^6/r_1^6$  from Eq. A.1, taking in to account that  $a \sim L$ , we see that for the first image terms

$$\begin{aligned} \mathfrak{R}_1 K_{P1} &\sim \mathcal{O}(L^2) \\ \mathfrak{R}_1 K_{P2} &\sim \mathcal{O}(L^4) \\ \mathfrak{R}_1 K_{J2} &\sim \mathcal{O}(L^3) \end{aligned} \quad (\text{A.5})$$



The  $K_{J_1}$  part is preserved by  $\mathfrak{R}_1$  so the first appropriate image of  $K_{J_1}$  is of the form  $\mathfrak{R}_2 K_{J_1}$  which is obtained from the above by exchanging labels  $1 \leftrightarrow 2$ . All higher order images continue to map  $r_1$  and  $r_2$  to  $\mathcal{O}(L)$  quantities. Because of this the higher order reflection terms are further rescaled only by additional factors of  $\frac{a}{L} \sim \mathcal{O}(1)$ . This means there will be an infinite series of terms with  $L$ -dependencies like those given in Eq. A.5. By Kulkarni's convergence proof it is also evident that the resulting coefficients on  $L^2$ ,  $L^3$ ,  $L^4$  must converge.

The key point is that there are no additional terms linear in  $L$  which result from symmetrization. Thus, the close approximation unsymmetrized  $\hat{K}_{ij}$  given in the text can equally be interpreted as the close approximation of the symmetrized  $\hat{K}_{ij}$ .

## References

- [1] K. Thorne, preprint **gr-qc/9704042**.
- [2] E. Flanagan, Talk given at the *15th International Conference on General Relativity and Gravitation*, Pune, India, 16-21 Dec. 1997, **gr-qc/9804024**.
- [3] S. Teukolsky, *Rev. Mod. Phys.* **71** S180 (1999).
- [4] The Binary Black Hole Grand Challenge Alliance: Gomez, R.; Lehner L.; Marsa, R.; Winicour, J.; Abrahams, A.; Anderson, A; Anninos, P.; Baumgarte T.; Bishop, N.; Brandt S.; Browne, J.; Camarda, K.; Choptuik, M.; Correl, R.; Cook, G.; Evans, C.; Finn, L.; Fox, G.; Haupt, T.; Huq, M.; Kidder, L.; Klasky, S.; Laguna, P.; Landry, W.; Lenaghan, J.; Masso, J.; Matzner, R.A.; Mitra, S.; Papadopoulos, P.; Parashar, M.; Rezzolla, L.; Rupright, M.; Saied, F.; Saylor, P.; Scheel, M.; Seidel, E.; Shapiro, S.; Shoemaker, D.; Smarr, L.; Szilagyi, *Phys. Rev. Lett.* **80** 3915 (1998).
- [5] The Binary Black Hole Grand Challenge Alliance: Gomez, R.; Lehner L.; Marsa, R.; Winicour, J.; Abrahams, A.; Anderson, A; Anninos, P.; Baumgarte T.; Bishop, N.; Brandt S.; Browne, J.; Camarda, K.; Choptuik, M.; Correl, R.; Cook, G.; Evans, C.; Finn, L.; Fox, G.; Haupt, T.; Huq, M.; Kidder, L.; Klasky, S.; Laguna, P.; Landry, W.; Lenaghan, J.; Masso, J.; Matzner, R.A.; Mitra, S.; Papadopoulos, P.; Parashar, M.; Rezzolla, L.; Rupright, M.; Saied, F.; Saylor, P.; Scheel, M.;

- Seidel, E.; Shapiro, S.; Shoemaker, D.; Smarr, L.; Szilagyi, *Phys. Rev. Lett.* **80** 1812 (1998).
- [6] R. Price, J. Pullin, *Phys. Rev. Lett.* **72** 3297 (1994).
- [7] J. York in L. Smarr, *Sources of Gravitational Radiation* (London, Cambridge University Press, 1979).
- [8] J. Bowen, J. York, *Phys. Rev. D* **21** 2047 (1980).
- [9] G. Cook 1990 Ph.D. thesis, University of North Carolina at Chapel Hill, Chapel Hill, North Carolina
- [10] G. B. Cook, *Phys. Rev. D* **44** 2983 (1991).
- [11] A. Abrahams, R. Price, *Phys. Rev. D* **53** 1963 (1996).
- [12] R. Gleiser, C. Nicasio, R. Price, J. Pullin, *Phys. Rev. D* **57** 3401 (1998).
- [13] S. Brandt, B. Bruegmann, Talk given at *8th Marcel Grossmann Meeting on Recent Developments in Theoretical and Experimental General Relativity, Gravitation and Relativistic Field Theories* (MG 8), Jerusalem, Israel, 22-27 Jun 1997, **gr-qc/9711015**.
- [14] C. Nicasio, R. Gleiser, R. Price, J. Pullin, *Phys. Rev. D* **59** 044024 (1999).
- [15] A. Zeferino, R. Price, *Phys. Rev. D* **56** 6336 (1997).
- [16] C. Misner, *Phys. Rev.* **118** 1110 (1960).
- [17] C. Cunningham, R. Price, V. Moncrief, *Ap. J.* **224** 643 (1978).

- [18] C. Cunningham, R. Price, V. Moncrief, *Ap. J.* **230** 870 (1979).
- [19] J. Baker, A. Abrahams, P. Anninos, S. Brandt, R. Price, J. Pullin and E. Seidel, *Phys. Rev. D* **55** 829 (1997).
- [20] J. Baker, C. B. Li, *Class. Quant. Grav.* **14** L77-L82 (1997).
- [21] A. M. Abrahams and G. B. Cook, *Phys. Rev. D* **50** R2364 (1994).
- [22] P. Anninos, R. H. Price, J. Pullin, E. Seidel and W.-M. Suen, *Phys. Rev. D* **52** 4462 (1995).
- [23] P. Anninos, D. Hobill, E. Seidel, L. Smarr, and W.-M. Suen, *Phys. Rev. Lett.* **71** 2851 (1993).
- [24] S. Chandrasekhar, *The Mathematical Theory of Black Holes* (New York, Oxford University Press, 1992).
- [25] W. Krivan, P. Laguna, P. Papadopoulos, N. Andersson, *Phys. Rev. D* **56** 3395 (1997).
- [26] W. Krivan, R. Price, *Phys. Rev. Lett.* **82** 1358 (1999).
- [27] W. Krivan, R. Price, *Phys. Rev. D* **58** 104003 (1998).
- [28] M. Campanelli C. Lousto, J. Baker, G. Khanna, J. Pullin, *Phys. Rev. D* **58** 084019 (1998).
- [29] J. Baker, R. Puzio, *Phys. Rev. D* **59** 044030 (1999).
- [30] A. Kulkarni, *J. Math. Phys.* **25** 1028 (1984).

Vita

John G. Baker

**Born:** February 21, 1969

**Nationality:** U.S. citizen

**Address:** Max-Planck-Institut für Gravitationsphysik, Albert-Einstein-Institut,

Am Mühlenberg, Haus 5,

D-14476 Golm, FRG

**Telephone:** Office: +49 331 567 70

**EMAIL:** baker@aei-potsdam.mpg.de

**Publications:**

*Collisions of Boosted Black Holes* J. Baker, A. Abrahams, P. Anninos,  
S. Brandt, R. Price, J. Pullin, E. Seidel, *Phys. Rev. D* **55** 829 (1997).

*The two-phase approximation for black hole collisions: Is it robust?*  
J. Baker, C. B. Li, *Class. Quant. Grav.* **14** L77-L82 (1997).

*The imposition of Cauchy data to the Teukolsky equation III: The rotating case* M. Campanelli, C. Lousto, J. Baker, G. Khanna, J. Pullin, *Phys. Rev. D* **58** 084019 (1998).

*New method for solving the initial value problem with application to multiple black holes*  
J. Baker, R. Puzio, *Phys. Rev. D* **59** 044030 (1999).